Neuromorphic analysis of hemodynamics using event-based cameras

Xavier Berthelon

Sorbonne Université

Ecole doctorale Sciences mécaniques, acoustique, électronique & robotique de Paris

Institut de la Vision – Equipe Vision et Calcul Naturel

Neuromorphic analysis of hemodynamics using event-based cameras

Thèse de Doctorat

par Xavier Berthelon

Dirigée par Pr. Ryad Benosman

Présentée et soutenue publiquement le 22 Novembre 2018

Devant un jury composé de :

Prof.	Jacques Duranteau	Rapporteur
Prof.	Claude Boccara	Rapporteur
Prof.	Stéphane Régnier	Examinateur
Associate Prof.	Guillaume Chenegros	Examinateur
Prof.	Ryad Benosman	Directeur de thèse

Time is an illusion. Look deep into nature, and then you will understand everything better.

– *Albert Einstein*

ABSTRACT

The micro-circulation plays a crucial role in the exchange of molecules between blood cells and organic tissues. Both acute and chronic illnesses can cause a degradation of the micro-circulatory network. The main alterations are characterized by a reduction of the velocity of red blood cells and perfusion density of capillaries. The understanding of such deregulation is crucial in the pathophysiology of many diseases. Despite the recent development of some technical devices to study the micro-circulation, there is no ideal tool to evaluate the micro-circulation at bedside. In this thesis, we present an innovative method which couples asynchronous time-based image sensors, built based on the working principle of the human retina, with medical imaging devices. Thanks to the high temporal resolution of these cameras, we estimate red blood cells velocities and densities within capillaries in real time and show for instance that during a hemorrhagic shock, our system estimates deregulation of the micro-circulation within minutes. Such a quick diagnosis could improve the evaluation of patients' states and real-time adaptation of hemodynamic treatments.

RÉSUMÉ

La micro-circulation joue un role essentiel dans l'échange de molécules entre le sang et les tissus. Certaines maladies aiguës ou chroniques peuvent altérer cette micro-circulation. Les dysfonctionnements sont alors caractérisés par une baisse de la vitesse des globules rouges ainsi que par une diminution de la densité de perfusion des capillaires. La compréhension de ces perturbations est essentielle dans la physiopathologie de nombreuses maladies. Malgré les avancées technologiques récentes, aucun outil n'est aujourd'hui disponible au chevet du patient pour évaluer l'état de la micro-circulation en temps réel. Dans cette thèse, nous présentons une méthode innovante associant une caméra évènementielle asynchrone, fonctionnant sur le même principe que la rétine humaine, à des dispositifs d'imagerie médicale. Grâce a la grande résolution temporelle de ces caméras, nous pouvons déterminer la vélocité et la densité des globules rouges dans les capillaires sanguins en temps réel. Nous montrons par exemple que durant un choc hémorragique, ce système est capable de détecter une détérioration de la micro-circulation en l'espace de quelques minutes. Cette évaluation rapide pourrait considérablement améliorer l'appréciation de l'état des patients et permettre une adaptation des traitements en temps réel.

PUBLICATIONS

1. "Full-field OCT technique for high speed event-based optical flow and particle tracking",
   X. Berthelon, G. Chenegros, N. Libert, J.A. Sahel, K. Grieve and R. Benosman,
   Optics Express 25, 12611-12621 (2017)

2. "Effects of cooling on the SNR and contrast detection of a low-light event based camera.",
   X. Berthelon, G. Chenegros, T. Finateu, S.H. Ieng and R. Benosman,
   IEEE Transaction on Biomedical Circuits and Systems (pending publication - 2018)

3. "A Spiking Neural Network Model of Depth from Defocus for Event-based Neuromorphic Vision",
   G. Haessig, X. Berthelon, S.H. Ieng and R. Benosman,
   Nature Communication (pending publication - 2018)

4. "Event-based study of the micro-circulation enables an early identification of a hemorrhagic shock.",
   X. Berthelon, G. Chenegros, N. Libert and R. Benosman,
   Science (under review - 2019)

CONFERENCES

1. Opticsvalley Seminar - "Technologies Photoniques : L'Imagerie pour le Biomédical", CHNO des Quinzes-Vingts, 28 rue Charenton 75012 Paris FRANCE, 29/11/2016
2. OSA Biophotonics Congress - "Optics in the Life Sciences", Sheraton San Diego Hotel Marina, San Diego California USA, 02/04/2017 - 05/04/2017
3. OSA Biophotonics Congress - "Biomedical Optics", The Diplomat Beach Resort, Hollywood Florida USA, 03/04/2018 - 06/04/2018 **Talk session**

ACKNOWLEDGEMENTS

Avant de plonger dans la jungle des équations, algorithmes et montages optiques qui constituent cette thèse, je tiens à vous faire par, en toute humilité, de mes impressions sur ces trois années de doctorat à l'Institut de la Vision. J'ai eu la chance de travailler dans une équipe innovante et stimulante tant par ses compétences transverses que par la bonne humeur des gens qui la constituent. Nous travaillons dans un domaine récent et innovant où tout est à faire. Si bien que parfois un mois ou deux de recherche se soldent par une impasse. J'ai trouvé cela très frustrant et même difficile au début. Les réorientations d'un sujet de thèse sont nombreuses et il est parfois difficile de voir où cela va aboutir. Mais au final je ne regrette rien du chemin parcouru.

Heureusement je n'étais pas seul... et je tiens à remercier toutes les personnes sans qui tout ce travail n'aurait pu être accompli. A commencer par mes parents, qui m'ont toujours encouragé et motivé. Merci pour tous ces week-end détente en Bourgogne qui m'ont permis de sortir la tête de Paris.

Je remercie Laura qui m'a soutenu et supporté pendant ces 3 années avec une attention sans égale.

Je remercie toutes les personnes qui m'ont accueilli dans ce labo et sont parties depuis: Camille, Quentin, Christophe, Sihem, David. Je remercie également tous mes collègues actuels, pour nos discussions et rigolades autour d'un café ou d'un verre dans l'un des nombreux bar du quartier.

Je remercie la team Arkose qui était présente dès 8h (et de bonne humeur) pour grimper des voies plus ou moins rouge... en particulier Germain, Paul, Kevin A. et Adrien qui sont devenus avec le temps bien plus que des collègues.

Je remercie Anne-Laure et Marine que j'avais un immense plaisir à voir à chacun de leurs passage à Paris.

Merci également à toutes les personnes avec qui j'ai eu la chance de collaborer: Nicolas Libert, Nathalie Oru, Kate Grieve, Thomas Finateu, Piotr Dudek et bien d'autres.

Enfin je remercie mes encadrants, et en particulier Ryad Benosman, pour avoir mis à ma disposition tous les moyens nécessaires pour faire de cette thèse un succès.

CONTENTS

ACRONYMS

ATIS Asynchronous Time-based Image Sensor

BSI Back Side Illumination

CT Computer Tomography

DFD Depth From Defocus

DFF Depth From Focus

DOF Depth Of Field

DVS Dynamic Vision Sensor

FFOCT Full-Field Optical Coherence Tomogrpahy

FPGA Field Programmable Gate Array

GEE Geometric Encircled Energy

MAP Mean Arterial Pressure

MRI Magnetic Resonance Tomography

NA Numerical aperture

OCT Optical Coherence Tomography

OPD Optical Path Difference

OPS Orthogonal Polarization Spectral

PCB Process Control Block

PSF Point Spread Function

PZT Piezoelectric accuator

RBC Red Blood Cell

RPM Rotations Per Minute

SDF Sidestream Dark Field

SNR Signal to Noise Ratio

VGA Video Graphic Array

INTRODUCTION

A DEEP UNDERSTANDING OF THE MICRO-CIRCULATION: A MEDICAL NEED

The cardiovascular system is the organ responsible for blood transportation to the entire body. Each day, the heart beats over 100 000 times and pumps around 7 500 liters of blood through a network of vessels 100 000 kilometers long. The primary function of this complex structure is to convey, via the red blood cells, oxygen, hormones, and nutrients to other organs in order to provide nourishment, help in fighting diseases, stabilize temperature, pH and maintain homeostasis. The cardiovascular system can be seen to function in two parts: a macro-circulatory network connected to a micro-circulatory network.

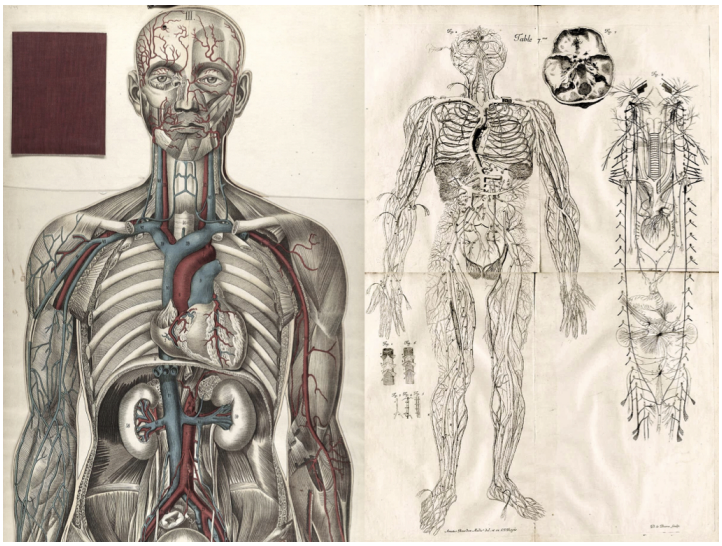

Figure 1: Human anatomical chart of blood vessels with major organs [1].

The microcirculatory network

The micro-circulation is the place for the exchange of molecules between erythrocytes and tissues. It is composed of a branching network of vessels classified as arterioles, venules, and capillaries. Adequate blood flow within this network is, therefore, an essential prerequisite for proper organ perfusion and function [65].

Many pathologies can lead to a deregulation of the micro-circulation [11]. On the one hand, chronic illnesses such as diabetes [42] or cardiovascular diseases [59] are known sources of abnormalities in the perfusion of micro-vessels. On the other hand, acute illnesses such as the different types of shock also contribute to a deterioration of

the micro-circulation [24, 62]. For instance, a direct consequence of a hemorrhagic shock is a sudden reduction of the blood volume [20] which rapidly leads to a degradation of the micro-circulatory network [40, 55, 61]. Dysfunctions are characterized by heterogeneous abnormalities in blood flow. Micro-vessels are in these cases non-perfused, hypo-perfused or on the opposite hyper-perfused locally [13, 24].

For several years now, many technical solutions have been developed to estimate the dynamic parameters of the micro-circulation with quantitative tools [18, 19, 46]. However, current technical solutions have major limitations in term of temporal or spatial resolution and are often subject to heavy off-line processing [67]. This prevents the use of micro-hemodynamic data to guide clinicians during resuscitation. This analysis is supported by the work of S. Eriksson *et. al* in "Non-invasive imaging of micro-circulation: a technology review" [17], which states that there is a growing need for medical imaging techniques which would allow a non-invasive study of blood flow. Ideally, the measurement should be *"fast to decrease vulnerability to motion artifacts and making it possible to study dynamic processes."*. The dynamic morphological parameters that are of interest are the following:

- Vessel density within the field of view,
- Rate of perfused vessels,
- Dynamic measurements of micro-circulatory blood flow velocity and blood cell concentration.

However, as mentioned in the study previously cited, no non-invasive technique today can determine blood flow parameters such as speed or cell density in-vivo with a high temporal resolution and real-time data processing. Current image acquisition methods either lack the required temporal resolution and can only measure global variables or they acquire sequences of frames at a high rate, thus requiring heavy off-line post-processing. To solve this issue, two solutions are therefore possible:

- First, increase the computing power in order to process a tremendous amount of information in real-time. This solution is the most straightforward but requires expensive, bulky, energy consuming processors. Such a quick fix is not worth considering.
- Second, increase the temporal resolution without increasing the data load. Frames recorded in medical imaging often carry much redundant information from the static components of the scene. A method that would acquire only the time-varying signal can drastically reduce the amount of information recorded and therefore allow an increase of the temporal resolution.

Event-based cameras

Event-based sensors have recently gained popularity as they record information in a sparse manner. These new bio-inspired cameras were designed according to the working principle of the human retina [12, 38, 39]. Most biological sensors, such as the human eye, are more efficient than their artificial counterparts. When dealing with daily tasks that involve real-time processing of the information, perception or motion control, they are orders of magnitude more energy-efficient. We have very little knowledge of the reason for this superiority, yet a possible clue might be the difference between the hardware architecture and style of computation between the biological systems and the state-of-the-art synchronous artificial sensors. Cameras have always been designed to record frames with a fixed sampling rate, while most biological sensors, such as the retina, handle the information in a sparse asynchronous fashion.

Studies on the human retina show that there are about a million retinal ganglion cells that exit the optic nerve. They are divided into two groups as described in [66]:

- The "Magno-cellular" system, which is oriented towards global detection, depth, and motion. These cells, represented on Figure.2 on the right side, have a large receptive field, short latency and generate transient responses to changes in a visual scene. This is referred to as the "where" system and represent about 20% of the retinal ganglion cells.
- The "Parvo-cellular" system handles the more detailed information such as color, texture or spatial information. Parvo-cells, represented on Figure.2 on the left side, are located mainly in the fovea and represent 80% of the retinal ganglion cells. Their receptive fields are smaller, but they have longer latency and compose the "what" system.

Conventional frame-based cameras can be associated with the Parvo-cellular system as they capture the detailed information of a visual scene but neglect its dynamic components mostly perceived by the Magno-cells. In an attempt to replicate how the "where" system works, a first line a dynamic vision sensors (DVS) [35, 36] has been developed. These neuromorphic cameras are composed of an array of fully independent and asynchronous pixels, sensitive only to light variations. However detailed information perceived by the Parvo-cells are here discarded. In order to combine both perceptions from the "what" and "where" systems, extensive work has led to the developement of a second generation of neuromorphic sensors called asynchronous time-based image sensors [52].

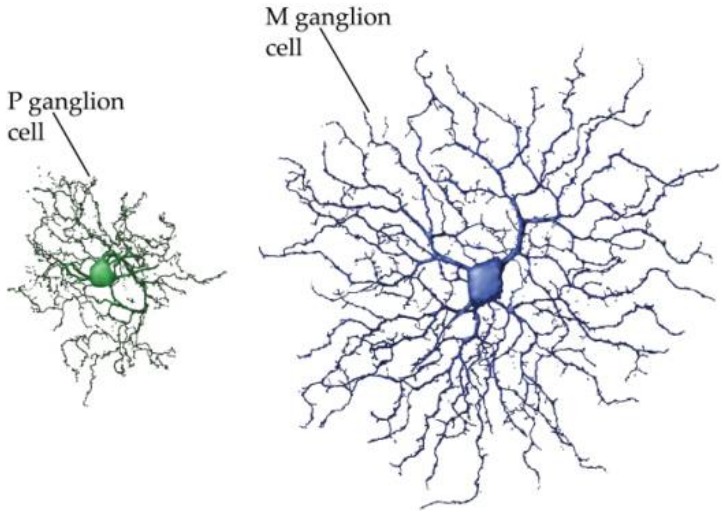

Figure 2: Left: Parvo-cell sensible to global detection, depth and motion. Right: Magno-cell, sensible to colors, textures and fine details.

An ATIS camera, shown on Figure.3.a, is an Asynchronous Time-based Image Sensor that detects relative changes in log pixel luminance over time. It is composed of a 304×240 array of asynchronous pixels. Each one of them has two coupled detection units:

- A change detector unit (PD2 on Figure.3.b) with a fill factor of 10% of the total pixel surface. This unit is a fast continuous logarithmic photoreceptor with asynchronous event-driven processing. A change of illuminance recorded will result in a change of the photocurrent I_{ph}. This photocurrent is monitored continuously and sent to two voltage comparators which generate ON and OFF events, as shown on Figure.3.c, when there is a significant increase or decrease of the photocurrent.

- An integrating PWM exposure measurement unit (PD1 on Figure.3.b) with a fill factor of 20% of the total pixel surface. This part of the pixel triggers a gray level value measurement whenever an event is created. The computation relies on a time integration of the incoming signal which is inversely proportional to the gray level value.

As soon as a variation of light is detected, the process of communicating this change event off-chip is initiated. Off-chip communication executes with low latency (on the order of microseconds), ensuring that the time at which a change event is read out from the ATIS inherently represents the time at which the change was detected. This asynchronous low-latency readout scheme provides the high temporal resolution change detection data. Let $e(\mathbf{p}, t)$ be an event occurring at time t at the spatial location $\mathbf{p} = (x, y)^T$. A positive change of contrast results in an ON event (polarity=+1), and a negative change of

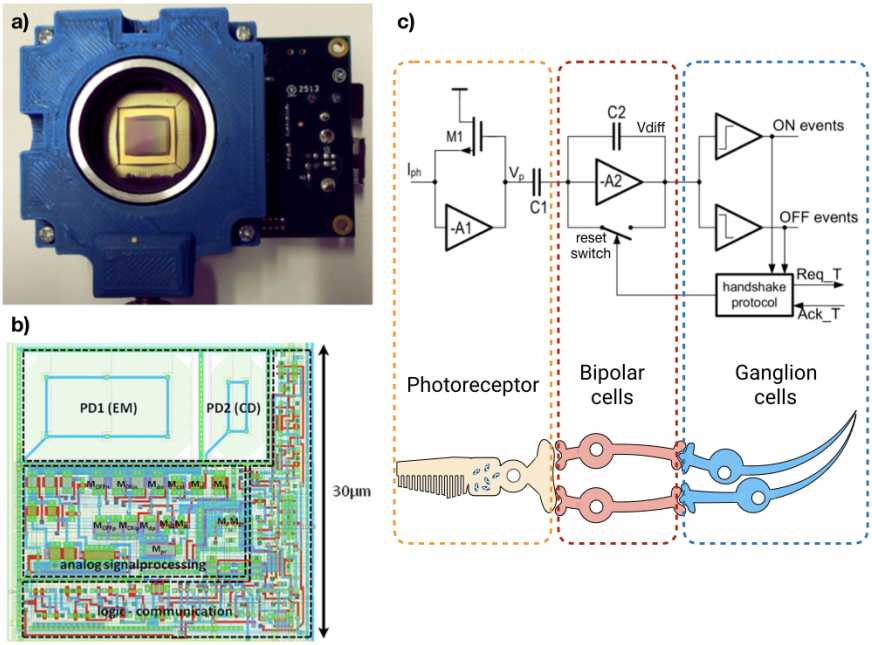

Figure 3: a) Picture of the Asynchronous Time Based Image Sensor. b) Single pixel layout. c) Pixel circuit and corresponding cells in the human retina. The voltage comparators on the right act as ganglion cells.

contrast in an OFF event (polarity=-1) as presented on Figure.4.

The threshold τ beyond which a change of luminance is high enough to create an event is tuned according to the scene. Smaller intensity fluctuations are not recorded and do not generate any event. Unlike for frame-based cameras, the redundant information is not recorded. For low contrasts, the value of parameter τ is decreased in order to detect smaller intensity variations.

On Figure.5 is shown a comparison between a frame-based acquisition with a fixed sampling rate and an event-based acquisition over time. The amount of information contained in both acquisitions is identical, yet the quantity of useful information contained in the event based recording is increased thanks to the greater temporal resolution.

The event-based acquisition paradigm allows us to go beyond the current conventional methods used in bio-medical imaging thanks to its high temporal resolution [50, 51]. A complete review of the history of these sensors can be found in [53].

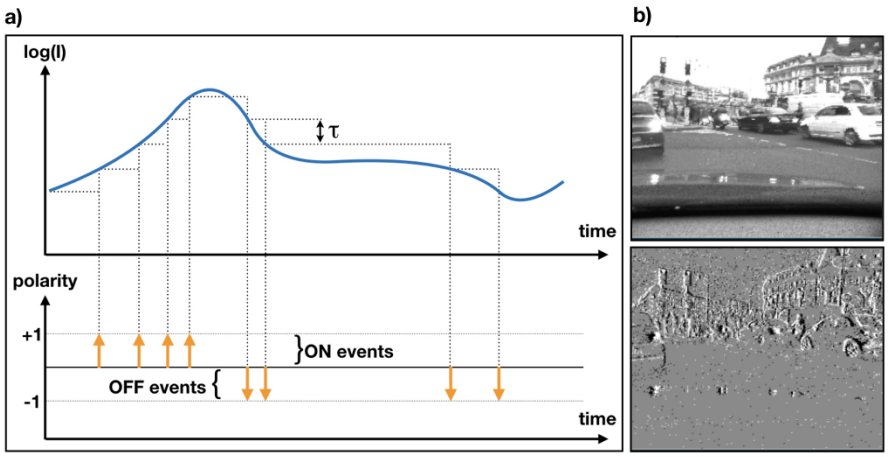

Figure 4: a) Detection principle of the Atis camera. b) gray level and event base representation of a scene over 500ms.

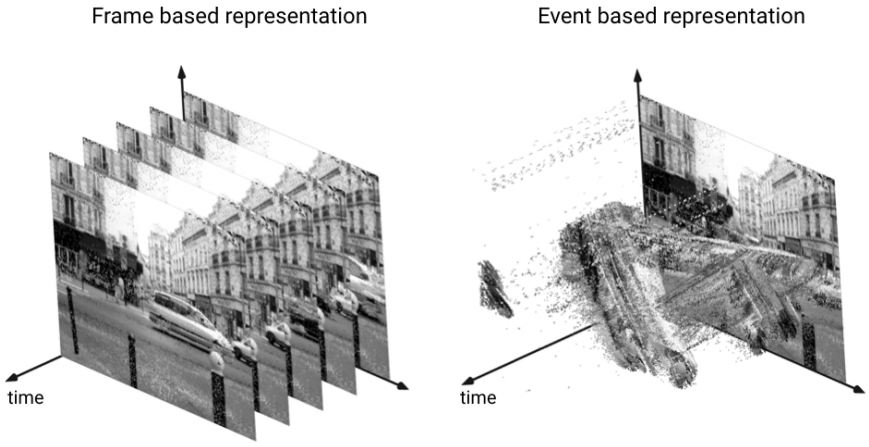

Figure 5: Comparison between a frame-based (left) and event-based (right) acquisitions.

Medical imaging

In order to observe dynamics at the cellular scale, we need to investigate the best candidate among today's medical imaging techniques. Current methods in the field of microscopy can be divided into two groups. The first one gathers macroscopic methods such as laser Doppler imaging [21], laser speckle imaging [32] or diffuse optical imaging [16] which have a large penetration depth but at the cost of a poor spatial resolution. Their resolution of hundreds of μm to mm is not sufficient to image individual cells. The second group is the microscopic techniques such as two-photon microscopy [9] or confocal microscopy that can reach a micron-scale resolution with a penetration depth of several tens of μm, a smaller field of

view ($200\mu m \times 200\mu m$) and offline image processing. Red blood cells imaging requires a technique with a micron-scale spatial resolution that can image in depth within a few hundred microns. Optical coherence tomography (OCT) methods offer a good compromise between a wide field of view, good spatial resolution and penetration depth [23, 25]. In particular, full-field optical coherence tomography (FFOCT), a variant of OCT, has been developed to provide a stack of *en-face* images in depth with a cellular resolution on biological samples [14, 15, 68]. This non-invasive technique requires no contrast agent and is conventionally used to image a variety of biological samples from the cornea and the retina to the brain or gastrointestinal tissues [41, 56, 73].

Conventional FFOCT has initially been developed to study static samples. Indeed, mathematical recombination of several frames is required in order to observe a single depth plan, and any dynamic artifact generates motion blur on the reconstruction. Recently though, studies have been carried out on motion estimation using OCT techniques. This includes Doppler-OCT which records shifts in frequency of laser radiation scattered by moving particles [30]. OCT angiography aims to suppress static scattering from the tissue sample, in order to keep only the dynamic scattering components [26]. Another technique is dynamic light scattering optical coherence tomography [28]. There is also OCT velocity techniques based on Mie scattering which aim to study red blood cell speed and flux [29]. More recently developed, dynamic full-field OCT (DFFOCT) is a technique used to reveal subcellular metabolic contrast by exploiting the time dependence of the interferometric signals [2]. However, these dynamic approaches are limited by the frame rate of the camera used which cannot go beyond several hundred frames per second (250-600 Hz) [26, 28–30, 58]. A large amount of acquired data generally prevents the estimate of velocities and direction of motion in real time for single particles [43].

For the first time, we propose in this work to couple an optical coherence tomography technique with an asynchronous sensor in order to image moving objects. Event-based vision has previously been used in microscopy to compute optical flow at several kHz [5] and to track micro-particles using an event-based Hough transform [44]. However, existing methods have been developed for transmission microscopy to operate on a single depth plane and only on ex-vivo, fluorescent, controlled samples. In the first part of this thesis, we show how the high temporal resolution and sparse nature of the data recorded by an event-based camera allow the observation of dynamic components at a microscopic scale with a FFOCT setup. The major challenge that has arisen is the sensitivity of the camera to

low contrasts with low levels of light. This has led to the development of a new generation of event-based sensors. We will see in the second part of this thesis how we improved our hardware. Firstly we designed a new version of the sensor and increased its signal to noise ratio (SNR) by reducing thermal noise. Additionally, we developed a portable micro-circulation device, less bulky than a complete FFOCT setup. This equipment is meant for a day to day use in care facilities to monitor the dynamic morphological parameters of micro-circulation, that is to say, the dynamic measurements of blood flow velocity and blood cell concentration. Finally, we will focus on the biological results in a small animal in-vivo. The event-based algorithms used for tracking and velocity estimation were initially design for robotic vision and the observation of biological samples called for an adaptation of our algorithms. We show that during a hemorrhage simulation, our method estimates abnormalities in the micro-circulatory network more quickly than any current technology. This allows an early detection of hemorrhagic shocks.

Part I

FULL-FIELD OCT WITH AN EVENT BASED CAMERA

1

PHYSICAL PRINCIPLE OF FFOCT

Optical Coherence Tomography (OCT) is an imaging method that captures micrometer-resolution images from a scattering sample. In the field of medical imaging devices, OCT and by extension its Full-Field version (FFOCT) fill a gap, both in terms of penetration depth and spatial resolution, as seen on Figure.6. Indeed, it can image structures in depth up to several hundred microns, thus surpassing confocal microscopy. The spatial resolution is however decreased and limited to samples in the order of 10µm for OCT and 1µm for FFOCT. Techniques such as Magnetic Resonance Imaging (MRI), Ultrasounds or High-resolution Computed Tomography (CT) scan, on the opposite, have a greater penetration depth but at the cost of a poorer spatial resolution.

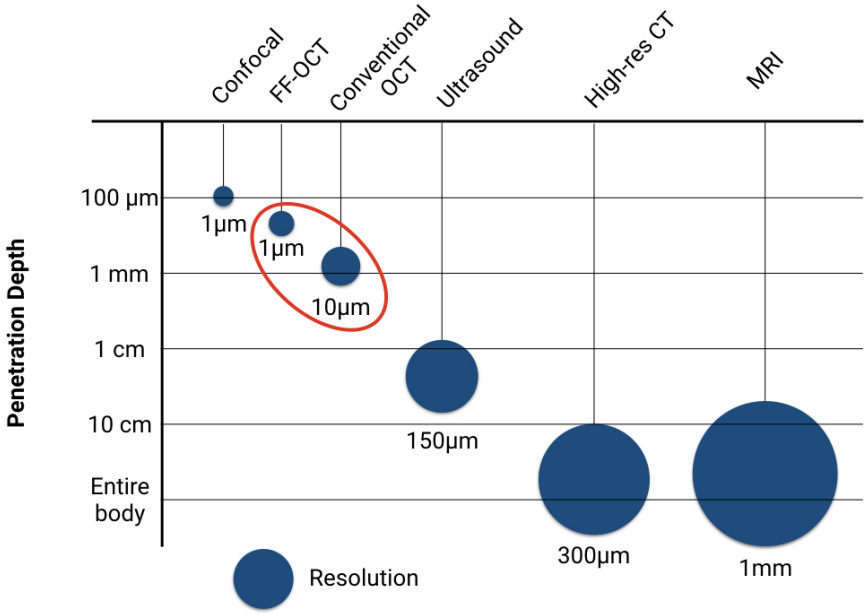

Figure 6: Spatial resolution and penetration depth of modern medical imaging techniques.

The OCT has, like ultrasounds, an acquisition time short enough to support tomographic imaging (imaging by section) at video rates. This makes OCT more tolerant to sample/subject motion than either CT or MRI. Additionally, OCT techniques are non-invasive and require no use of external contrast agents. The method relies on non-ionising radiations at biologically safe levels which enables long exposure times. Last point of comparison, the complexity of OCT, closer

to ultrasounds than it is to CT or MRI, makes it possible to design relatively low-cost and portable scanners.

1.1 INTERFEROMETRY AND OCT

OCT works similarly to ultrasound, with light waves instead of sound. The light sent to the sample is back-scattered at different depths. The time-delay from the reflected light wave is used to reconstruct a depth profile of the sample structure. Due to the high velocity of light compared to sound waves, time delays cannot be measured in the same fashion. Therefore OCT methods rely on interferometry, which uses waves superimposition, to determine these delays. The initial light beam is divided in half and sent to both the biological sample and a flat reflecting component called the reference mirror. Thanks to its wave-like properties, the back-scattered light that has traveled the same optical path in both arms can interfere. In other words, waves with identical frequencies and phase will add each other while waves with opposite phases will cancel out as seen on Figure.7.

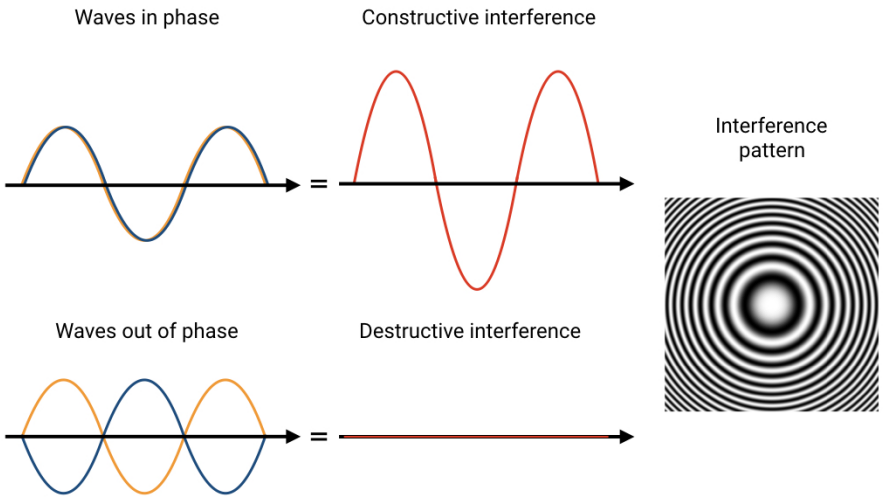

Figure 7: Principle of constructive and destructive interferences. Two waves in phase add with one another and two waves out of phase cancel out. The resulting interference pattern is an alternate of bright and dark stripes.

The time delays correspond to the phase shifts in the interference pattern. With a perfectly coherent (single frequency) light source, we observe alternating black and white patterns as shown on Figure.7. This region where interference occur is called the coherent length

and is inversely proportional to the spectral width of the light source. In other words, a monochromatic light source has an infinite coherent length while a completely incoherent light source has an infinitely small coherent length. OCT uses a broad spectrum light source as the axial resolution of this imaging technique is governed by the coherent length of the illumination. Initially, the first setups were using superluminescent diodes providing a 10 to 15μm axial resolution.

1.2 FULL-FIELD OPTICAL COHERENCE TOMOGRAPHY

In FFOCT, a stack of en-face images is captured by the camera. The light source is incoherent, and the microscope is based on a Linnik interferometer, that is to say, a bulk Michelson interferometer with two immersion microscope objectives in both arms, as seen on Figure.8. In addition to a conventional Michelson interferometer, the optical path length, as well as the focusing in both arms, can be adjusted individually. Axial and transverse resolutions are independent in FFOCT and can be separately optimized as follow:

- The numerical aperture (NA) of the microscope objective defines the transverse resolution. In conventional OCT, cross-sectional (x,z) images are obtained by scanning the beam in the transverse direction (x). Therefore a large depth of field is necessary, at least equal to the size of the image in depth (z). Low-NA objectives must be used which limits the transverse resolution. In FFOCT, as en-face images are directly recorded, high-NA objectives can be used, thus increasing the transverse resolution to $1,5\mu m$.

- Axial resolution is governed by the coherent length of the light source, which is inversely proportional to the spectral bandwidth. With incoherent light source, FFOCT benefits from a spectrum width of several hundred nm which yields a theoretical axial resolution of $0,7\mu m$ in water. However, the axial resolution may be degraded by dispersion mismatch when imaging in depth inside tissues.

In order to reconstruct a full 3D volume, the sample is translated step by step (one μm) in the axial direction (z). At each depth, the tomographic signal is extracted by computing the amplitude of the interference signal using the principle of phase-shifting interferometry. In other words, the tomographic image is obtained by a mathematical combination of at least two frames with a known phase shift between the images. Our setup is using a four images reconstruction method. To create the modulation, the mirror in the reference arm is attached to a piezoelectric actuator (PZT) that oscillates to generate a phase

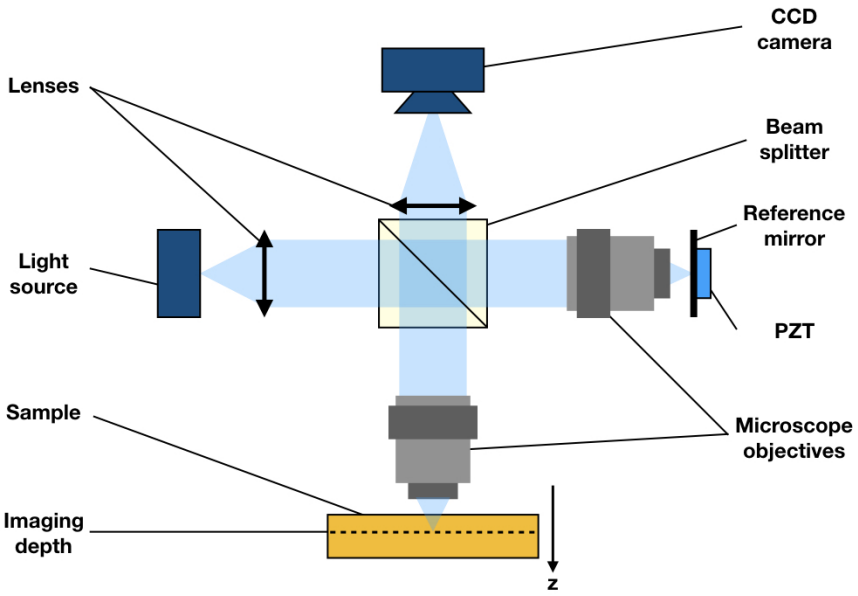

Figure 8: Full-field OCT principle using a Linnik interferometer. The light source is sent to both the reference arm and the sample. Light backscattered by the sample that has traveled the same optical path length as in the reference arm interferes. The signal is captured by a CCD camera and the sample is scanned along the z axis for a full volume reconstruction.

shift of $\pi/2$. The signal on the CCD camera is the sum of the interference image formed by the uniform image of the reference mirror and the sample's image upon which is superimposed the incoherent light from reflections and backscattering from different depths of the sample. Without any modulation, the intensity I on a pixel (x, y) is

$$I(x, y) = I_0(x, y) + A(x, y)\cos\phi(x, y), \tag{1}$$

with I_0 the average of the intensity, A the amplitude of the interference signal and ϕ the phase difference between light waves from the sample and the reference mirror. To get rid of the background illumination, a know phase shift is introduced by the PZT. The time-varying intensity on the pixel (x, y) becomes

$$I(x, y, t) = I_0(x, y) + A(x, y)\cos[\phi(x, y) + \beta\sin(2\pi f t + \alpha)], \tag{2}$$

with β the amplitude of the induced phase shift, α a relative phase and f is the frequency of the modulation. For a single tomographic image, we record four frames with a fixed phase shift, giving different

interference patterns as seen on Figure.9. A CCD camera is synchronized with the PZT and driven at a frequency $4f = 4/T$ to acquire one image for each phase shift.

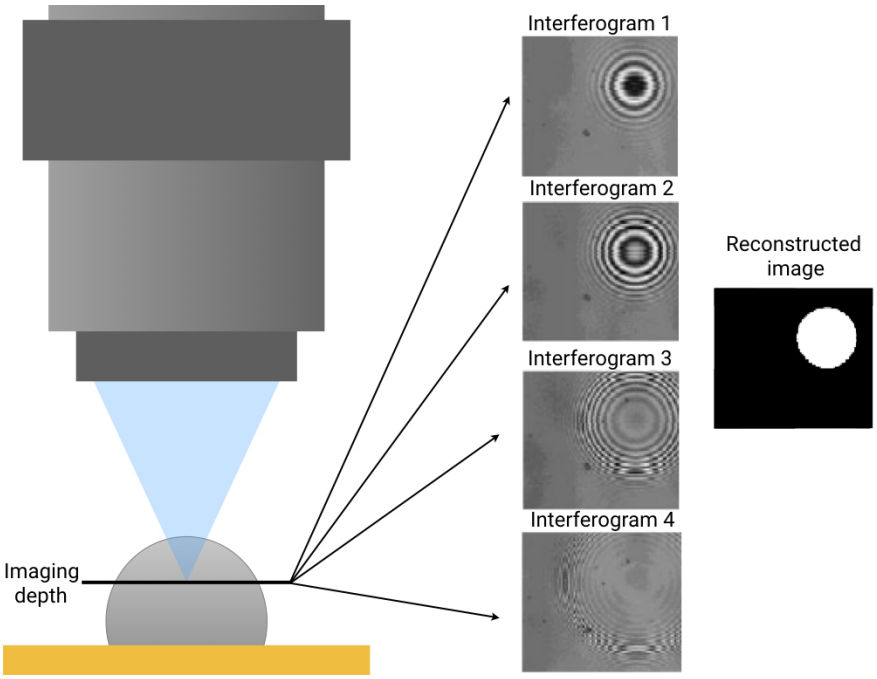

Figure 9: Four consecutive interference patterns acquired for a single depth image. The phase shift induced by the PZT in between the image is known which enables a tomographic reconstruction (slice image on the right) thanks to a mathematical recombination of the images.

In practice, a set of N series of four images is acquired and accumulated in order to increase the signal to noise ratio of the interferometric images before their recombination. The signal on a pixel of these accumulated images (E_1, E_2, E_3 and E_4) is the integration of the signal $I(x, y, t)$ over the four quarters of the modulation period:

$$E_i(x, y) = N \int_{(i-1)T/4}^{iT/4} I(x, y, t)dt, \qquad i = 1, 2, 3, 4. \tag{3}$$

Thanks to a mathematical combination of the images E_i, we can compute the signal $A(x, y)$. By tuning both the modulation amplitude of the PZT (β) and the relative phase (α) [15] we get the following relation:

$$A^2(N/2f)^2 \simeq (E_1 - E_2 - E_3 + E_4)^2 + (E_1 - E_2 + E_3 - E_4)^2. \tag{4}$$

This represents the tomographic image at a given depth.

1.3 COUPLING OF THE ATIS WITH THE FFOCT MICROSCOPE

We previously stated that FFOCT has initially been designed for static imaging only. Dynamic FFOCT is booming right now [2, 31, 64], yet the process of phase-shifting interferometry requires the combination of several interference images which does not tolerate well sample motion. Current cameras used in this field are limited to frame rates of 250 to 700Hz. After the four frames association, this corresponds to a maximum imaging rate of 60 to 175Hz. Conventional CCD sensors used in OCT have pixels with a pitch of $5\mu m$. In order not to suffer from motion blur, the same object has to be imaged on the same pixel within the acquisition time of the four frames. Let us assume that the acquisition rate is 700Hz, corresponding to an imaging speed of 175Hz. Then the object must not travel more than $5\mu m$ at the sensor plan during the $6ms$ of a single frame acquisition. In FFOCT, the microscope objectives used are $\times 10$ water immersion objectives. This gives a traveling distance of $0.5\mu m$ at the sample level. As a result, the maximum speed that can be recorded without motion blur in FF-OCT is $0.08mm/s$ which is rather slow compared to the typical speed of erythrocytes inside capillaries: around $3mm/s$ [10]. Ultra-high speed cameras such as those manufactured by Hamamatsu can record up to thousands of frames per second, however it often is on a buffer of the camera and the amount of information to deal with is substantial. The transfer of data as well as the processing takes time and is energy intensive.

Another issue of silicon-based CCD cameras is their full well capacity (FWC) which is rather low. The FWC defines the amount of charge an individual pixel can hold before saturating and is a crucial parameter in detection sensitivity. To compensate for this low FWC, N images are often accumulated as described in the previous section. This limits even more the acquisition speed which gets divided by the number of accumulations.

The incoming signal on the camera in FF-OCT is the sum of the interferometric signal and the intensity of the static background signal, i.e. the light that does not interfere. This background signal is time independent. Therefore, when using an event based camera, only the variations in the interferometric signal at a given depth are recorded in the form of events. A scan can then be performed along the z-axis to image different planes inside a 3D volume.

In conventional FF-OCT imaging, a piezoelectric chip is used to move the reference mirror and create a phase modulation to reconstruct images from a mathematical combination of several frames. When studying dynamic movements, such a reconstruction induces

motion blur as objects are not imaged on the same pixel on two consecutive frames. With our method, we track only the movements of the pattern of interference with an event-based camera. We tune the value of τ, which is the detection threshold for event-based cameras, so that the changes of intensity coming from objects outside the coherence volume (the area where the interfering light is back-scattered) are below this threshold and do not generate events. The value of τ strongly depends on the imaging depth and will be fine-tuned accordingly.

Event-based cameras detect significant amplitude changes, enabling scene driven acquisitions. Their strongest advantage compared to frame based devices is their increased temporal resolution as no redundant information is recorded. When dealing with the output of a FFOCT microscope, only the time-varying signal related to the pattern of interferences will be recorded. In the next chapter of this thesis, we will perform experiments with this setup and assess its performances with two algorithms: an event-based optical flow and a tracking algorithm. We will investigate if the recording of the dynamics of the pattern of interference alone is enough to measure a velocity in depth, as well as a density of particles, and what are the physical limitations of this setup.

2 MICRO-CIRCULATION MODEL

We designed a micro-circulation model with a microfluidic chip and calibrated micro-particles. The aim of this setup is to analyze the flow and density of particles inside a volume in real time with the event-based camera. The reasons why we needed at first a micro-circulation model are the following:

- Due to hardware constraints on the FFOCT setup, it was easier to start with a sample that can be easily controlled and used repeatedly in order to develop and test our algorithms.
- The spatial resolution of the ATIS camera as well as the size of its pixels reduce the field of view and limit the observation of tiny structures given the microscope objectives provided with the FFOCT device.
- A precisely controlled sample was necessary in order to properly calibrate the camera and test its performances when pushed to the limits.

2.1 EXPERIMENTAL SETUP

We adapted a commercially available FFOCT scanner (LLTech SAS) as shown on Figure.10. The microscope lenses used are $\times 10$ water immersion lenses with a 0.3 N.A. The resolution of the system is $1.5\mu m$ lateral and $1\mu m$ axial.

Figure 10: Full-field OCT device from LLTech SAS.

The event-based camera has a resolution of 304×240 pixels, which represents a field of view of $0.72 \times 0.91\text{mm}$. A PMMA microfluidic chip (provided by MicroFluidic ChipShop) with a channel of section $S = 2500\mu\text{m} \times 150\mu\text{m}$ is set under the microscope objective to observe red polyethylene microspheres, as shown on Figure.11. The diameter of these micro-particles ranges from $30\mu\text{m}$ to $45\mu\text{m}$ and they flow in a 0.1% Tween solution. We control the flow with a plastic syringe filled with a solution of water and calibrated micro-particles and connect it to a syringe pump. This syringe pump provides a ground truth flow with a maximum error of 0.1ml/h. From this ground truth we deduce the theoretical average speed in the field of view according to the equation:

$$v_{avg} = \frac{Flow}{ChannelSection} \tag{5}$$

At any depth inside the channel the expected velocity of particles is given by $v = v_m(1 - \frac{r^2}{R^2})$ with $v_m = 2v_{avg}$, the maximum velocity at the center of the channel, r the radial coordinate (equal to zero at the center of the channel) and R the radius of the channel ($150\mu\text{m}$). Close to the edges, the particles are almost at a standstill, and in the middle of the channel the velocity is maximum.

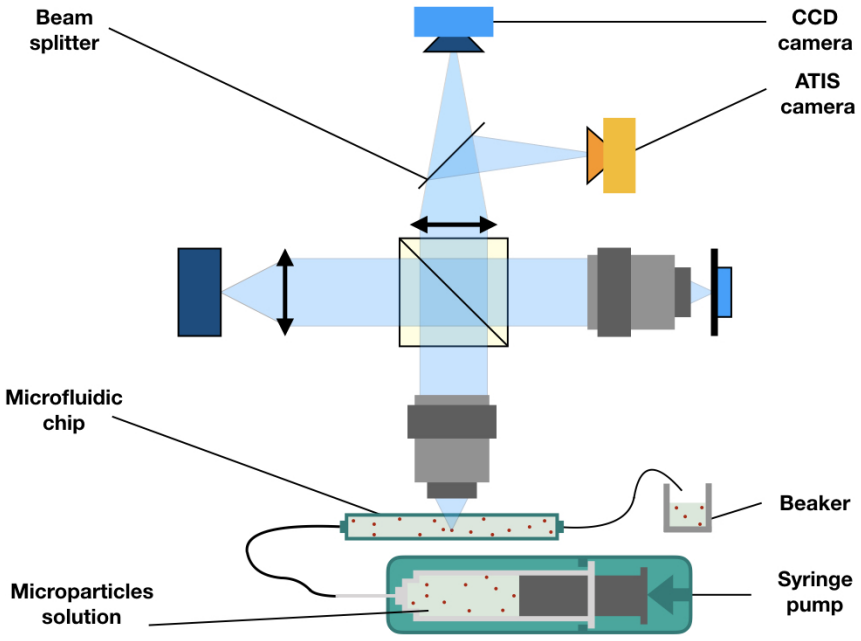

Figure 11: Schematic representation of the FF-OCT microscope coupled with the ATIS camera together with a microfluidic chip and syringe pump.

We perform a set of experiments for which we record the optical flow and density of particles at a depth of 50, 70 or $100\mu\text{m}$. This corresponds to the typical depths of the very first blood capillaries in the

human body. The influence of the imaging depth on the results will be further discussed. On Figure.12 is shown a spatiotemporal representation of events (in blue) generated by moving particles inside the channel of the microfluidic chip. The vertical axis represents the time and the two other the xy plane.

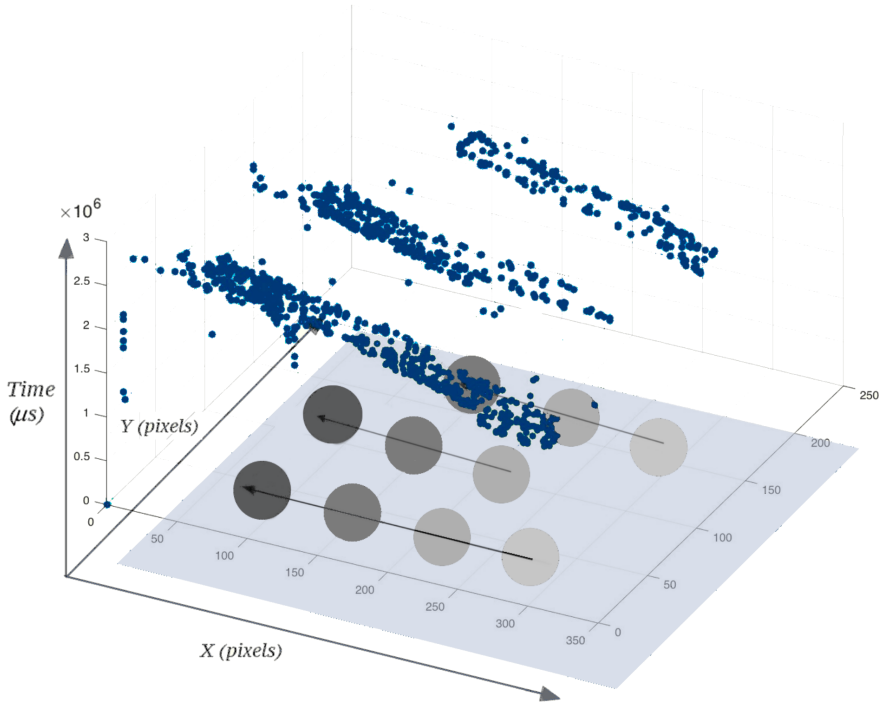

Figure 12: 3D visualisation of events generated over time by the movement of small particles (grey circles moving from right to left). The vertical axis is the time, the other two are the xy plane. The blue dots are both positive and negative events.

2.2 MEASURE OF THE OPTICAL FLOW

Optical flow represents the distribution of apparent velocity of objects in an image. The optical flow of an object is characterized by a vector whose norm is proportional to the speed and whose angle is related to the direction of the object's movement. Before putting equations on the table let us visualize in a simple way how the event-based optical flow is computed.

Let us assume that pixel A on Figure.13 triggers an event at time T_1. We then have a look at the behavior of the pixel's direct neighbors (B, C, D, and E) during a short period of time. If another pixel (for instance B) generates an event at time T_2, we can compute the first vectorial component of the optical flow, which is inversely proportional to the time lapse in between the two events. If a second neighbor (for

instance E) triggers an event during the observation period, we get a second vectorial component for the flow. Their combination gives the local optical flow vector.

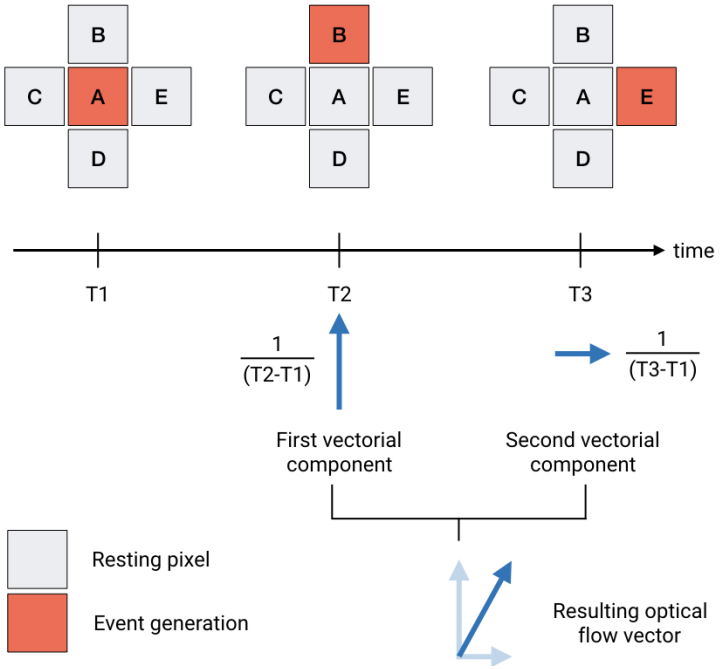

Figure 13: Principle of the optical flow computation. After pixel A triggers an event, we observe its neighbors. The following first two events generated give the vectorial components of the optical flow vector which are inversely proportional to the time lapse between events.

We now generalize the methodology previously described through the adaptation of an event based visual flow algorithm [6] for which a function Σ_e, as shown on Figure.14, maps to each event $\mathbf{p}$ its time t:

$$\begin{aligned} \Sigma_e : \quad \mathbb{N}^2 &\to \mathbb{R} \\ \mathbf{p} &\mapsto \Sigma_e(\mathbf{p}) = t \end{aligned} \tag{6}$$

The surface of active events Σ_e is derived to provide an estimation of the orientation and amplitude of the motion. If we consider a small displacement $\Delta\mathbf{p}$ from the location $\mathbf{p}$ we can write:

$$\Sigma_e(\mathbf{p}+\Delta\mathbf{p}) = \Sigma_e(\mathbf{p}) + \nabla\Sigma_e^T \Delta\mathbf{p} + \circ(\|\Delta\mathbf{p}\|) \tag{7}$$

with $\nabla\Sigma_e = (\frac{\partial\Sigma_e}{\partial x}, \frac{\partial\Sigma_e}{\partial y})^T$. The principle of the event based optical flow algorithm conventionally uses a continuous formulation of the time surface enveloppe of events. As expected, the camera provides a discrete information of spatial locations in the form of events. However for better clarity and generalization purposes we will use partial derivatives. Both partial derivatives are functions of a single variable

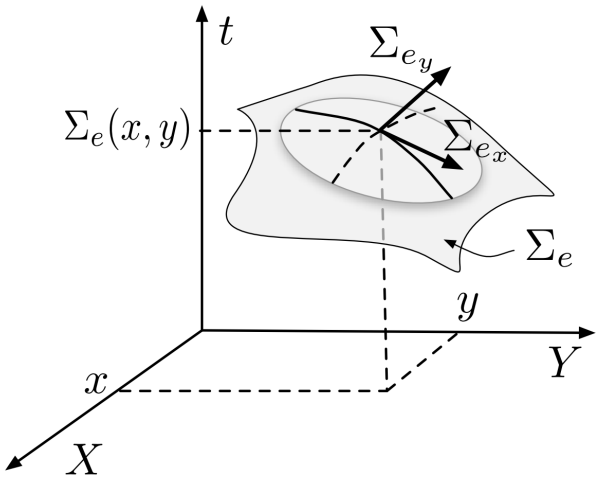

Figure 14: Illustration of the principle of the optical flow computation. The surface of active events Σ_e provides an estimate of the amplitude and direction of motion.

x or y and, as time is a strictly increasing function, the derivatives of the surface Σ_e are never equal to zero at any point. The inverse function theorem can therefore be used around the location $\mathbf{p} = (x, y)^T$.

$$\begin{aligned} \frac{\partial \Sigma_e}{\partial x}(x, y_0) &= \frac{d\Sigma_e|_{y=y_0}}{dx}(x) = \frac{1}{v_x(x,y_0)} \\ \frac{\partial \Sigma_e}{\partial y}(x_0, y) &= \frac{d\Sigma_e|_{x=x_0}}{dy}(y) = \frac{1}{v_y(x_0,y)} \end{aligned} \tag{8}$$

with $\Sigma_e|_{y=y_0}$ and $\Sigma_e|_{x=x_0}$ the values of Σ_e respectively restricted to y and x. We obtain the inverse pixellic velocity of events V.S. time, thus providing both the rate and the direction for every incoming event in *s/pixels*:

$$\nabla \Sigma_e = \left(\frac{1}{v_x}, \frac{1}{v_y}\right)^T. \tag{9}$$

This information allows us to represent the optical flow of the event at location $\mathbf{p} + \Delta\mathbf{p}$ by a vector (v_x, v_y). The current limitation of this approach is the 2D velocity detection although it may be computed in multiple planes. This method, however, shows great potential for a 3D absolute velocity reconstruction providing that the v_z component of the speed is given.

In a first experiment, we estimate the performances of our system on speed measurement.

On Figure 15 is shown data from an event-based recording of microparticles moving from right to left, all in the same direction and at the same speed. The arrows represented on the events are the computed optical flow vectors (v_x, v_y) described in the previous section.

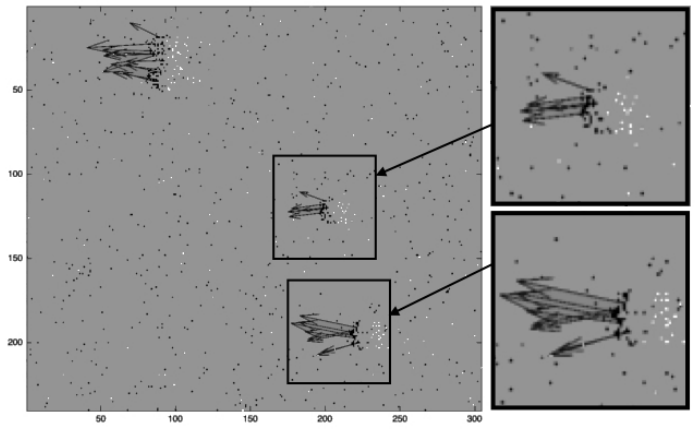

Figure 15: Optical flow for particles moving from right to left over a time window of 15ms. Both axes on the left image are the x and y plane. The black and white dots represent negative and positive events respectively.

The flow is laminar with a maximum Reynolds number of 4.1 and ranges from 0.1ml/h to 9ml/h. We estimate the optical flow on a set of 20 recordings lasting 1 minute each for various values of the flow at a depth of 50µm and 100µm. The expected speed at these depths is identical and ranges from 0.4mm/s to 6.7mm/s.

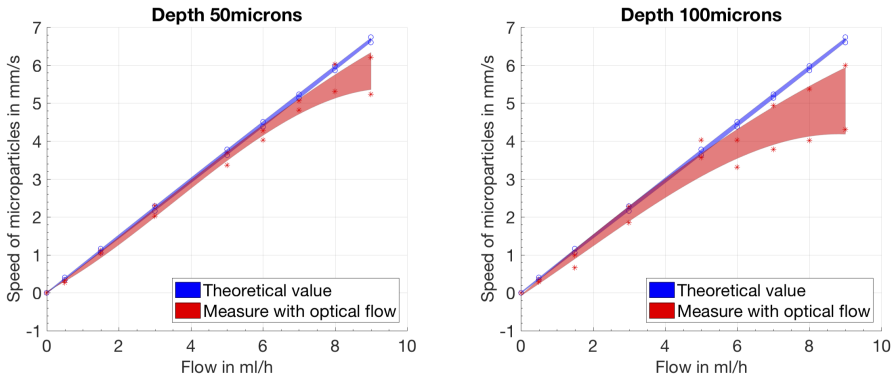

Figure 16: Speed of microparticles according to the flow at 50µm on the left and 100µm on the right. In blue, the theoretical speed according to the rate of the syringe pump, in red the estimated speed. The shaded areas on both curves correspond to the measurement error. Results divert from the ground truth above 6.5ml/h at 50µm and above 4.5ml/h at 100µm.

Figure 16 shows the theoretical value of particle speed in blue and the estimated optical flow in red, in the horizontal direction. We compute the measurement error from the ground truth, provided by the syringe pump, and estimate it using the averaged squared deviation for the optical flow. At 50µm deep, the estimated speeds for particles below 6ml/h is close to the ground truth with a maximum difference of 6%. At 100µm deep, the estimated speed for particles below

4.5ml/h is close to the ground truth. The influence of depth on the accuracy will be further discussed. In general, the measured speeds are smaller than the ground truth, as friction forces inside the fluid are not accounted for in the ground truth. At any time, as particles are free to move in any direction inside the channel, they may enter or leave the coherence volume. Particles moving in the axial direction have a different speed than particles staying within the coherence volume. Indeed their horizontal component is smaller. However, these particles cross the coherence volume at high speed thus appearing on a tiny time scale in the data and do not affect our computation since the number of occurrences detected is lower than 4%. The process reaches its limits at 6.5ml/h where velocities are too high even for the event-based camera to trigger a significant change of contrast.

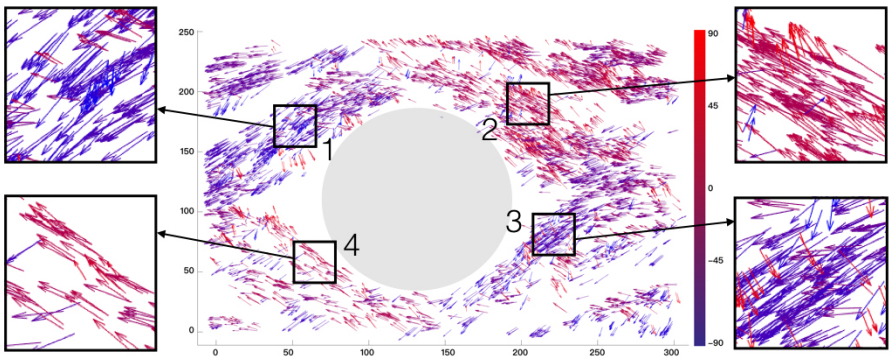

Figure 17: Map of the optical flow around an air bubble (grey circle). The two axes are the x and y plane. Each arrow represents the mean velocity of a particle at a given time accumulated over a time window of two minutes. The color bar represents the angle of the optical flow vector from 90 degrees to -90 degrees.

Figure 17 shows a map of the visual optical flow accumulated over two minutes for particles flowing around an air bubble (grey circle) created inside the channel of the microfluidic chip at 50µm in depth. Each arrow represents the optical flow of a single particle at different positions during a two minutes recording. Their color depends on the angle of the optical flow vector which varies between 90 degrees (red) and -90 degrees (blue).

Figure 18 shows the values of the local angle and norm of the optical flow for each square of Fig. 17. The error is computed using the averaged squared deviation. The standard deviation for the norm of the optical flow in square 4 has a higher value due to the low number of vectors inside this region.

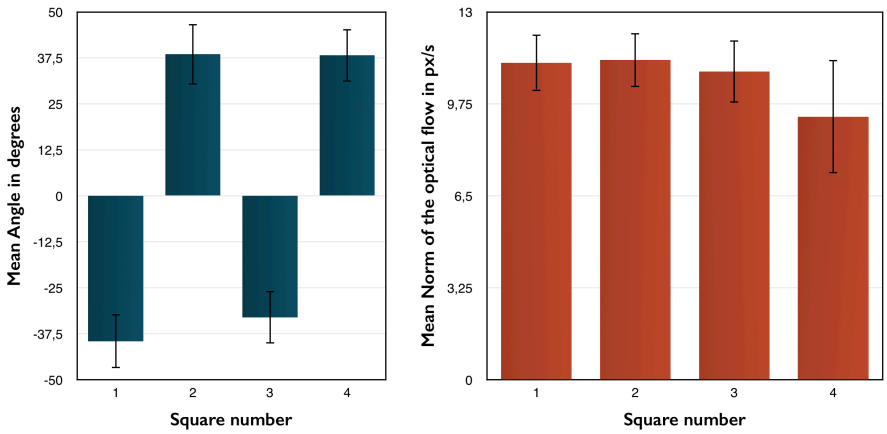

Figure 18: On the left, the mean angle value of the optical flow inside each square. On the right, the mean norm of the optical flow inside each square.

2.3 DENSITY OF PARTICLES

Visual tracking using event-based sensors has been widely developed for macro-applications in broad daylight [47, 54]. A moving object generates a cloud of events that represent the spatial distribution of the observed shape. If we assume that these events are normally distributed, we can mathematically represent the cloud of events by a bivariate normal distribution $\beta(\mu, \sigma)$ [27], where μ is the current location of the tracker and σ the covariance matrix that determines the size and orientation of the tracker:

$$\sigma(t) = \begin{bmatrix} \sigma_x^2(t) & \sigma_{xy}(t) \\ \sigma_{xy}(t) & \sigma_y^2(t) \end{bmatrix} \tag{10}$$

Every incoming event will affect the gaussian tracker's shape and position so that it best fits the event cloud's spatial distribution. When an event occurs, the probability that it belongs to an existing tracker i is given by:

$$P_i(\mathbf{p}) = \frac{1}{2\pi}|\beta_i|^{-\frac{1}{2}} e^{-\frac{1}{2}(\mathbf{p}-\mu_i)^T \beta^{-1}(\mathbf{p}-\mu_i)} \tag{11}$$

with $\mathbf{p} = (x, y)^T$ the spatial position of the event. When the probability is above a predefined threshold, the tracker with the highest probabilty updates its location (μ) as follows:

$$\mu = \alpha\mu + (1-\alpha)\mathbf{p} \tag{12}$$

where α is an update factor set experimentally according to the mean number of events of a considered scene. We define the activity A of a tracker as:

$$A_i(t) = \begin{cases} A_i(t-\Delta t)e^{-\frac{\Delta t}{\delta}} + P_i(\mathbf{p}), & \text{if } e(\mathbf{p},t) \in tracker_i \\ A_i(t-\Delta t)e^{-\frac{\Delta t}{\delta}}, & \text{otherwise.} \end{cases} \quad (13)$$

with Δt the time difference between current and previous events and δ the temporal activity decrease. A tracker can be in either of these three states (as shown on Figure.19):

- inactive : its activity is low and the tracker is not visible
- active : its activity is high, the Gaussian blob is following an object and is visible
- paused : its activity is not high enough to appear visible, however the tracker updates its position with incoming events

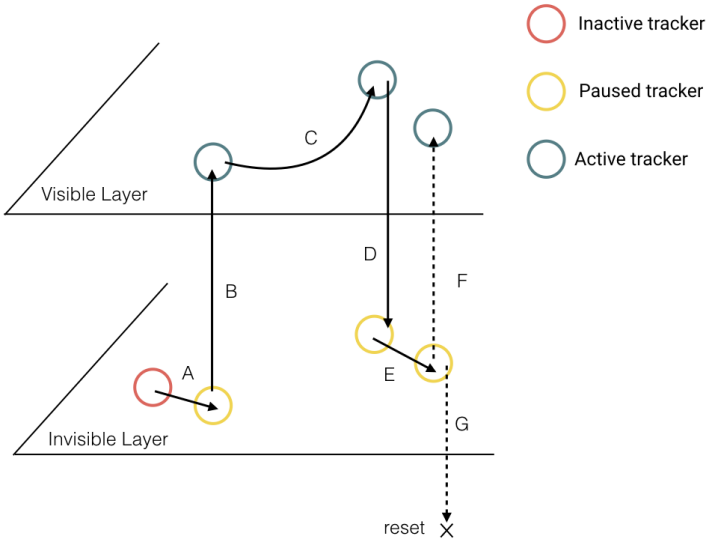

Figure 19: Activation scheme of trackers. (A) A tracker is initialized with a set of parameters. (B) It starts following an event cloud. (C) If its activity is sufficient, the tracker becomes active and switches to the visible layer. (C) The tracker follows the event cloud. (D) When the activity decreases, the tracker is switched back to the hidden layer. (E) It still updates its position according to the event cloud. Depending on the activity, the tracker may become visible again (F) or is deleted (G).

The Gaussian blob tracking algorithm allows the estimation of a particle density and therefore counting the number of particles in a solution (Fig. 20).

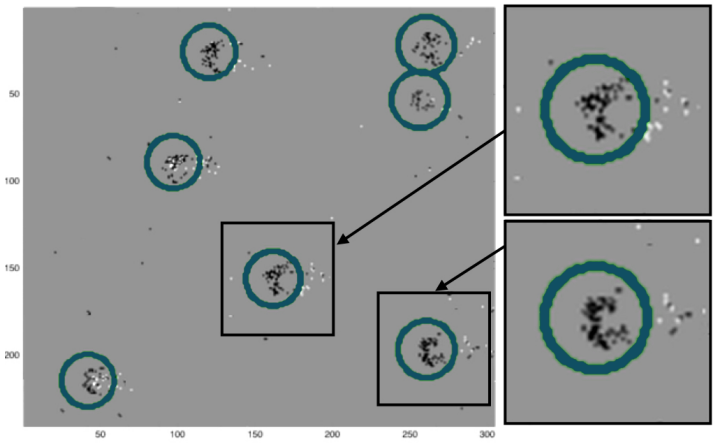

Figure 20: On the left, Gaussian blob tracking for microparticles over a time window of 20ms. The axes are the x and y plane. The black and white dots represent negative and positive events respectively. On the right are zooms on two particles. The blue circles represent the active blobs which are tracking microspheres.

We used solutions with different concentrations varying from 9 000 particles/ml to 28 000 particles/ml. The flow rate and the number of particles per ml are known, and we assume that, given the laminar flow, the particles are evenly distributed inside the channel of the microfluidic chip. We can therefore compute the theoretical concentration in microparticles within our coherence volume which will be our ground truth. Figure 21 shows results for five different concentrations. For each experiment the flow is set to 2ml/h, representing a movement of 3mm/s at a depth of 70µm.

Since we know that particles move in the same direction, we can count them using the number of active trackers that cross virtual vertical lines in the field of view. This operation is performed over ten lines across our image, giving a robust estimate of the number of particles. For high concentrations of microspheres i.e. more than 30 000 particles/ml, we tend to miss particles when they overlap with one another, and only one tracker becomes active for the pair. We have a difference of 10% or more with the ground truth.

It is important to emphasize that the chosen speed of 3mm/s at around 70µm corresponds to the natural velocity of blood cells inside capillaries. This is the target application of this work as conventional cameras cannot estimate velocities beyond 1.8mm/s for single particles at a microscopic level even with offline processing.

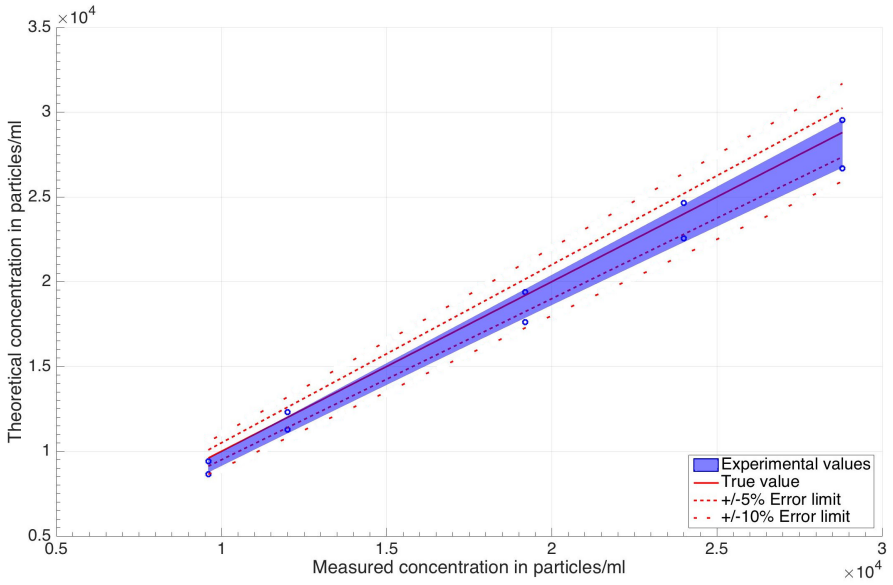

Figure 21: Density of -particles measured for different concentrations. In blue is the measured density of particles per ml. The red lines represent the error to the true value.

2.4 INFLUENCE OF DEPTH AND COMPUTATIONAL COST

The maximum penetration depth of the FF-OCT setup varies between 200 to 1000μm , depending on the sample (specifications provided by LLTech SAS). The resolution degrades with depth for imaging in scattering media because of the coherent detection of multiply scattered light. This is a common phenomenon in all OCT imaging systems. The interferometric signal becomes weaker as the imaging depth increases. The value of τ, previously introduced in section 2.2, defines how sensitive to contrast differences the pixels are. When the signal becomes weaker, the value of τ has to decrease in order to generate events when smaller light variations occur. As a consequence, we raise the SNR and results divert from the ground-truth. On Fig. 22 is shown the mean error of our measurements regarding the theoretical value for the flow (blue line) and the density of particles (red line) for a set of 10 recordings at the depths of 0, 50, 100 and 150 μm in a scattering medium (water with a drop of milk). We observe that we have an error above 10% when imaging deeper than 120μm for our experiments. However, our aim is to image blood capillaries which can be found within the first 100μm of the human tissues.

We set a time interval Δt_b containing a certain number of events. Let Δt_c be the computational time required to process our algorithms using the content of the first time interval. We can set an efficiency ratio r such as: $r = \frac{\Delta t_c}{\Delta t_b}$. If $r < 1$ the computation can be performed in real time. We cut all the data from the experiments at 4ml/h into

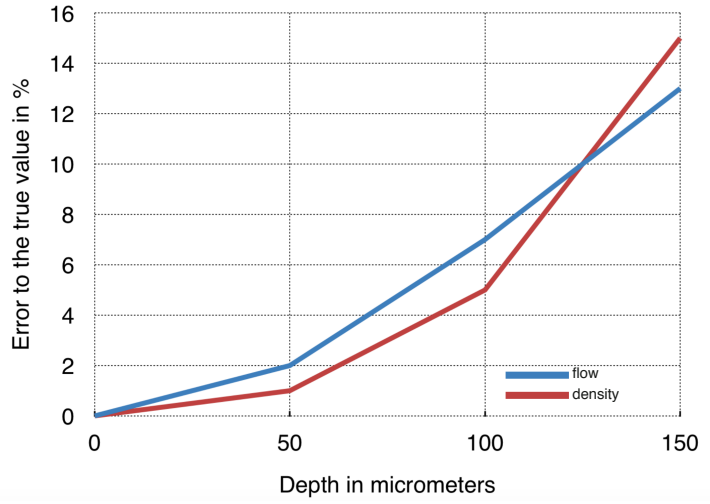

Figure 22: Error regarding the reference value for the optical flow (blue line) and the particle density (red line) depending on the imaging depth. For depths greater than 120µm this error exceeds 10% of the reference value.

time bins of $\Delta t_b = 100ms$. On Fig. 23 is shown in blue the number of events per bin and in red the corresponding efficiency ratio.

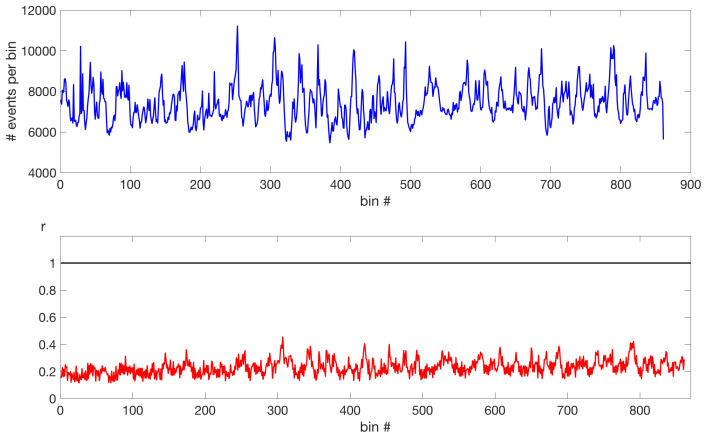

Figure 23: Top: in blue is the number of event per bin for the experimental data at 4ml/h. Bottom: in red is the computational ratio r. The maximum value is 0.45 and the mean value is 0.23 indicating a real time computation.

On average, the mean number of events per bin of 100ms is 7440, and the efficiency ratio is equal to 0.231, meaning that we can process data on average 4.3 times faster than real time. From this data, we estimate the mean processing time for a single event : 3.1µs. This gives a theoretical upper limit for online processing of 32000 events per bin of 100ms beyond which the information cannot be processed in real time anymore. However, this number of events per bin is way above

the typical values obtained with our recordings.

The work presented here has been supported by the European Research Council Helmholtz (ERC) (610 110, Synergy grant), and results have been published in 2017 in Optics Express [7].

SUMMARY

The theory for red blood cell study has now been fully established with the association of an event-based device and a medical imaging technique. We have just shown that the combination of FF-OCT with an event-based sensor allows the capture of fast-moving objects with high accuracy at a depth up to $120\mu m$. The low data rate allows tracking and motion estimation in real time at the native resolution of the sensor at low computational costs for flows as high as $6.5ml/h$ and velocities of $4.5mm/s$, going beyond existing limitations of the FF-OCT and other medical imaging techniques for this application. Currently, the camera's sensitivity to low contrasts limits the observation of smaller structures of interest such as red blood cells in-vivo.

Indeed when the particles exceed $6.5mm/s$, the change of illumination is not high enough to trigger an event, although the limit in the temporal resolution of the camera is not reached. The useful signal is drowned in the noise, and fine-tuning of the detection threshold is not possible anymore to retrieve only light variations from the interferometric signal.

The two possible solutions are the following: increase the signal or reduce the noise.

- Increasing the signal would require a stronger illumination. This is not a viable solution as biological samples can suffer from photo-bleaching or heat up and deteriorate due to a powerful light source.
- Reducing the noise means reducing the number of random pixels that trigger events when no light variations occur. The main source of noise with an event-based camera is thermal noise.

In the next part of this thesis, we will detail the development of a new type of asynchronous sensors, more sensitive to low contrasts. In a first part, we will take a look at the Helmtest camera which was developed with a cooling system. The aim of this prototype is to assess whether or not thermal noise has a significant impact on the signal and needs to be reduced. In the meantime, we realised that a complete FFOCT setup is bulky and cannot be used in daily routines at the patients' bedside for monitoring. We developed a compact handheld device to study hemodynamics related to the micro-circulation.

Part II

HARDWARE DEVELOPMENT TOWARDS MICRO-CIRCULATION IMAGING

3

DEVELOPMENT OF A COOLED EVENT-BASED SENSOR

3.1 LOW LIGHT HELMTEST CAMERA

The primary source of noise in conventional cameras is thermal noise, also known as Johnson-Nyquist noise. It represents the electronic artifacts generated by the agitation of the charge carriers. As a result, the electrons within the photo-diode are more likely to cross the energy barrier without the help of any energy from the photons. These electrons are responsible for noise events. A reduction of the temperature forces electrons to cross their energy barrier only when a sufficient amount of energy from the photons is transmitted. For this reason, high-speed frame-based cameras are often cooled down in order to reduce this agitation and increase their signal to noise ratio. We will investigate in this chapter if the same behavior occurs with event-based sensors and highlight, if there is any, the benefits of using a cooling system for noise reduction.

The Helmtest camera shown on Fig.24.a and Fig.24.b is an asynchronous camera composed of a 62×62 array of fully independent pixels.

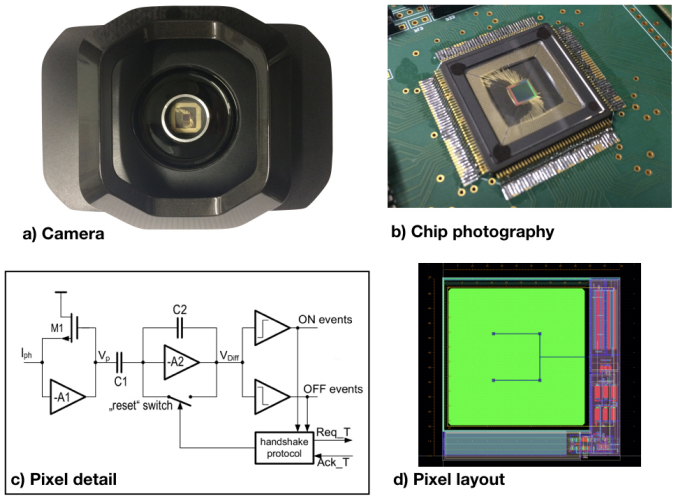

Figure 24: a) Helmtest camera, b) photography of the Helmtest chip on the PCB, c) electronic detail of the pixel, d) layout of the low light pixel.

These pixels were designed in a similar fashion to the ATIS camera with an increased fill factor. Each one is a change detector unit with a $60\mu m \times 60\mu m$ pitch. While the photosensitive area previously occupied 11% of the pixel's surface, it is now 60%.

Each pixel has a *change detector* unit. This unit, shown on Fig.24.d, is a fast continuous logarithmic photo-receptor with asynchronous event-driven signal processing. Its working principle is similar to the ATIS camera: a change of illuminance results in a change of the photo-current. This photo-current I_{ph} is continuously monitored and sent to two voltage comparators which generate ON and OFF events when there is a significant increase or decrease in the photo-current.

For the characterization of this sensor we used a modular integrating sphere from Thorlabs shown on Fig.25. The light source is a warm white 570mW LED which spectrum ranges from 400nm to 800nm as shown on Fig.26. The homogeneity of the light pattern is guaranteed at 2% and the output light power is controlled using a Thorlabs power-meter.

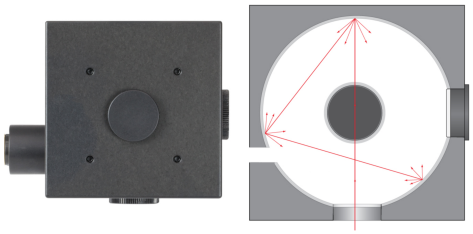

Figure 25: Modular integrating sphere from Thorlabs.

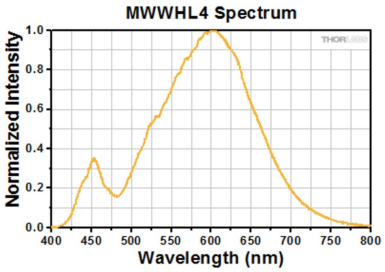

Figure 26: Spectrum of the warm white LED used for the experiments.

Low light conditions are often encountered in microscopy, which is the reason why we developed this new sensor. We use for the characterization of the camera two different illuminances:

- A *low illumination* of 2lux.
- A *high illumination* of 10lux.

These two levels of light are the lowest values at the sensor plan in respectively reflection and transmission microscopy that we measured in our setups.

We ensure that the sensor is well illuminated and at a fixed distance from the integrating sphere. The LED is supplied with DC current in order to avoid any blinking artifact, and its power is controlled with an external generator that sends rectangular type signals at a frequency of 200Hz. In this respect, we can precisely control the time variations of the illuminance.

We study here the event-probability after a homogeneous brightness change. The event probability $P(evt)$ is defined as the ratio between the number of times a pixel was triggered during a set of simulations $N_{trigger}$ and the number of simulations N_{simu}:

$$P(evt) = \frac{N_{trigger}}{N_{simu}} \tag{14}$$

It may happen that some pixel generate more events than they should for instance when they are defective. In this case, the probability is often much higher than 1. The frequency at which the change of illuminance occur is 200Hz, therefore, the frequency of the polarity inversion in a stream of events for one pixel should not exceed this value (ON events for the increase of illuminance followed by OFF events). In practice, due to noise, this value may exceed this upper limit. However, we assume that the pixels which record inversions of polarity more than two times above the upper limit over time are defective. Those faulty units will be discarded for this study.

We define the contrast variation Θ as the % of illuminance change with respect to an initial background. In other words:

$$\Theta = \frac{|I_2 - I_1|}{I_1} \tag{15}$$

with I_1 the background illuminance and I_2 the illuminance after the change of contrast. Again, this contrast ranges between 0 when the light level remains the same to 1 when the scene is completely dark or when the new illuminance is twice as bright (maximum value in this study). We noticed consistent results no matter if the variations are an increase or decrease of the base light level. The results presented in this paper are for an increase of the light level.

For the Atis camera, the event probability vs. contrast variation has been measured in [49] at different light levels including 2lux and 10 lux as shown on Figure.27.

In this study, we set the detection threshold τ previously introduced in Chapter.2 to its minimum value in order to detect the smallest contrast variations possible. The value of n enables the detection of contrast variations down to 10%. Any further reduction of this threshold results experimentally in a massive increase of the noise and a complete loss of the signal no matter if the cooling system is on or off. This is due to the physical parameters of the electronics used in the sensor.

Plotting the event probability vs. contrast variation would result in an ideal noise-free world in a step function: 0% to 100% with an infinite slope when the minimum detection threshold is reached. It

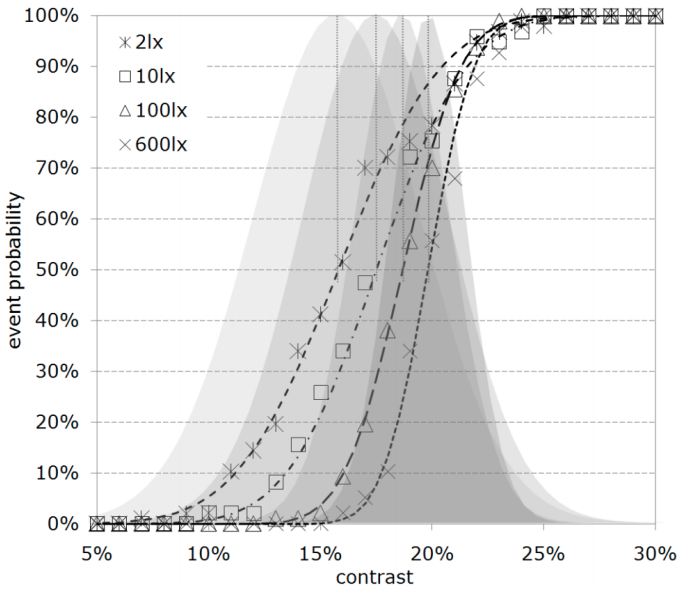

Figure 27: Response of the sensor in % for the ATIS camera for different variations of contrast. This image is taken from [49]

turns out that the real data are described by an "S-shaped" curve due to noise. The steeper is the slope, the closer it is to a noise-free acquisition. On Figure.27 we see that the slope of the curve decreases with the background light level. In other words, when reaching low light levels, the recordings are more noise polluted. We will investigate now how we can reduce this noise when recording variations of contrast by using the Helmtest camera and a Peltier based cooling system.

3.2 DESCRIPTION OF THE COOLING SYSTEM

In order to reduce thermal noise, we add at the back of the sensor a cooling system with two Peltier coolers, as seen of Figure.28, together with a radiator and a fan for convection. The Peltiers are stacked together using thermal glue, and a hole in the FPGA is enabling direct contact between the sensor and the coolers.

The Peltier effect is characterized by the creation of a cooling/heating effect at the junction of two materials when an electrical current flows through a circuit consisting of two different semiconductors. The Peltier effect can be considered as a counterpart to the Seebeck effect: in a closed thermoelectric circuit, the Seebeck effect will drive a current. This current will in turn (by the Peltier effect) systematically transfers heat from the hot to the cold junction as shown on Figure.29. By creating a current flow with an external power source, one can force displacement of the charge carriers within the semiconductors and therefore control the temperature difference between

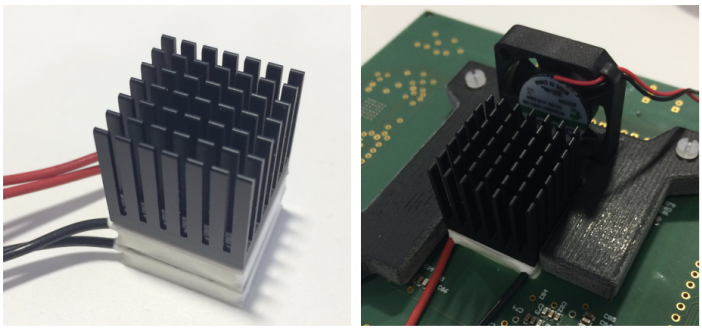

Figure 28: On the left is a stack of 2 Peltiers coolers mounted with a radiator in order to maximize heat dissipation. On the right is the system mounted on the PCB with a small fan to force convection.

the two surfaces. The greater is the current, the more critical the heat transfer is. This effect is increased when two different semiconductors are used.

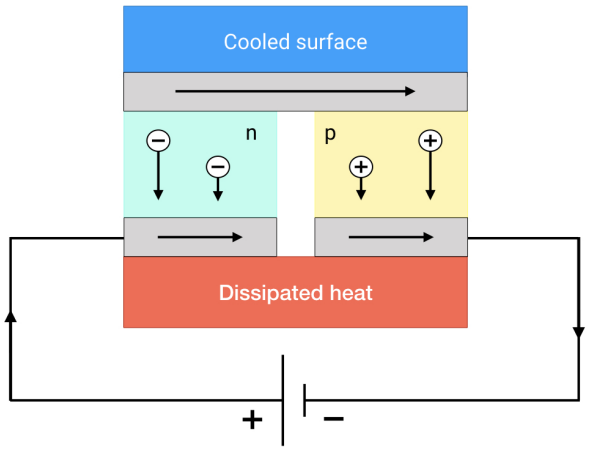

Figure 29: Physical principal of the Peltier effect where an external source of power forces a current flow in a closed thermoelectric circuit thus generating a heat transfer from the cold side to the hot side.

Although the temperature difference generated by the Peltier effect can be computed other phenomenon such as Joule heating or thermal gradient may influence the absolute value on the cold or hot side. In order to be accurate, we will measure for our experiments the temperature with a probe located at the junction between the sensor and the Peltier.

In order to look at the effect of the cooling system on the pixels' responses, we need to investigate in a first time if there is an optimal cooling temperature. It is characterized by the following points:

- An improvement of the signal to noise ratio thanks to the reduction of thermal noise.

- The absence of condensation on our device, that is to say, a cooling temperature above the dew point.

To determine the dew point, we need to measure the relative humidity around the sensor. We use for that a psychrometer system where two thermometers (dry and wet) measure the room temperature. The disparity between the temperatures measured gives an estimate of the relative humidity. Here, the temperature with the dry thermometer is 20.1° while it is 10.4° with its wet counterpart. From a standard psychrometric chart, this indicates a relative humidity of 28% [22].

We now compute the dew point temperature T_r as follow:

$$T_r = \frac{b\alpha(T, R_H)}{a - \alpha(T, R_H)} \tag{16}$$

with $b = 237,7°$, $a = 17,27°$ and α a function of the room temperature T and the relative humidity R_H defined by:

$$\alpha(T, R_H) = \frac{aT}{b + T} + \ln(R_H) \tag{17}$$

The dew point is here 1.1° which sets the limit for the cooling system beyond which condensation will start to appear on the sensor.

The best cooling temperature is when the signal to noise ratio is the greatest. Let's measure this signal to noise ratio (SNR) value for a range of power supplies to the Peltier coolers from $0W$ to $16W$. We define the SNR as the ratio between the number of $evt/\mu s$ of the global signal N_{signal} divided by the noise level N_{noise}:

$$SNR = \frac{N_{signal}}{N_{noise}} \tag{18}$$

The noise level N_{noise} is the number of events generated each micro-second without any signal, in other words without light variations, in the scene. We first measure this noise under low illumination and then observe a fast rotating fidget spinner under the same light conditions. The speed rotation of the fidget spinner is externally monitored with a motor in order to be identical during each experiment and the temperature at the back of the sensor is controlled with a probe. Between each acquisition, the current supply of the Peltier system is adjusted and we wait for the temperature to stabilize before recording. On Fig.30 are shown the values of the SNR and the sensor temperature according to the power supply.

We see that the temperature decreases with the power supply up to $9W$ after which it rises again. This is due to a lack of heat dissipation in our system. The hot side of the Peltier coolers prevents any further reduction of the local temperature. As expected the SNR is maximum

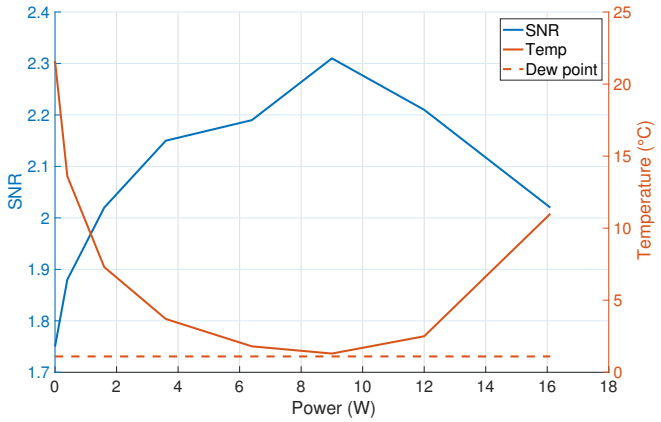

Figure 30: In orange is the temperature at the sensor plan in degrees, depending on the power supply in watts. The green curve is the corresponding SNR and the blue curve delimits the dew point.

right before we reached the dew point. We will therefore cool down the sensor to 1.5° when performing experiments with the cooling system.

With the example of the fidget spinner, we have at 1.5° a noise level of $0.57 evt/\mu s$ while it is $0.87 evt/\mu s$ when the cooling system is off. This gives a 30% attenuation of the noise level. With the activation of the Peltier coolers, the SNR was raised by a factor of 1.3.

Let us now focus on the effect of the cooling system on noise reduction alone for different levels of illuminance. On Table.1 we see the results for both a low and higher illuminance. In both cases, N_{noise} drops by 30% with the activation of the Peltier coolers.

Table 1: Effect of the cooling system on the number of noise events.

	Low illuminance		Higher illuminance	
	Regular	Cooled	Regular	Cooled
N_{noise}	0.18	0.125	0.082	0.058
Std	8%	9%	9%	12%

In another experiment we investigate the effect of cooling the sensor on signal detection for a set of contrast variations. As previously done, we study the event probability for the Helmtest camera under a low and higher illuminations with variations of contrast ranging from 0% to 50%. The results are displayed on Fig.31 and Fig.32 with a smoothing spline fitting curve model.

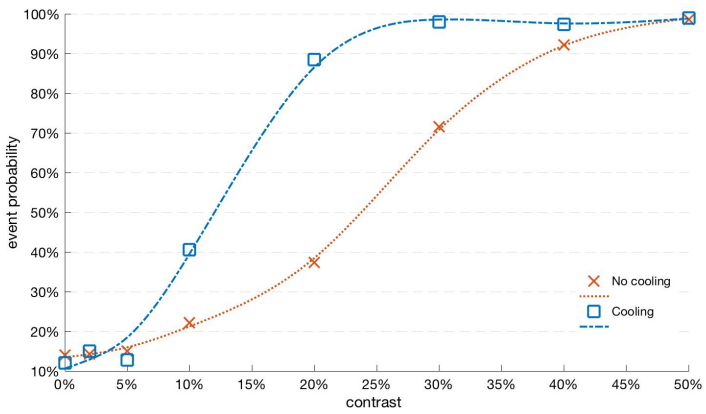

Figure 31: Event probability vs. stimulus contrast for a low level of light.

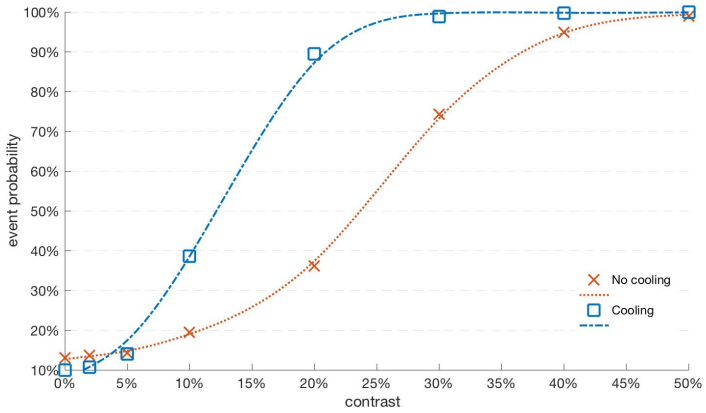

Figure 32: Event probability vs. stimulus contrast for a high level of light.

Without the cooling system, we see that the "S-shaped" curves have a slight slope meaning that the recordings are noise polluted. When the sensor is cooled down, the event probability is raised, and the detection function becomes closer to a step function. We gain in detection sensitivity by cooling the sensor.

3.3 EXPERIMENTAL RESULTS

We now test the effect of the cooling system on a practical application of event-based optical flow computation, which is often used in microscopy to estimate particle velocity and direction of motion.

We record for this experiment a rotating fan, shown on Fig.33, and compute the optical flow angle and norm [6] at the upper edge of the blade under low light conditions. On Fig.36 is the optical flow computed at 275 rotations per minute (RPM) with the cooling system on and off. The color of the flow represents the value of the vector's angle: from dark blue for 0 degrees to yellow, 360 degrees. At first glance, we clearly see that the optical flow seems less disrupted and

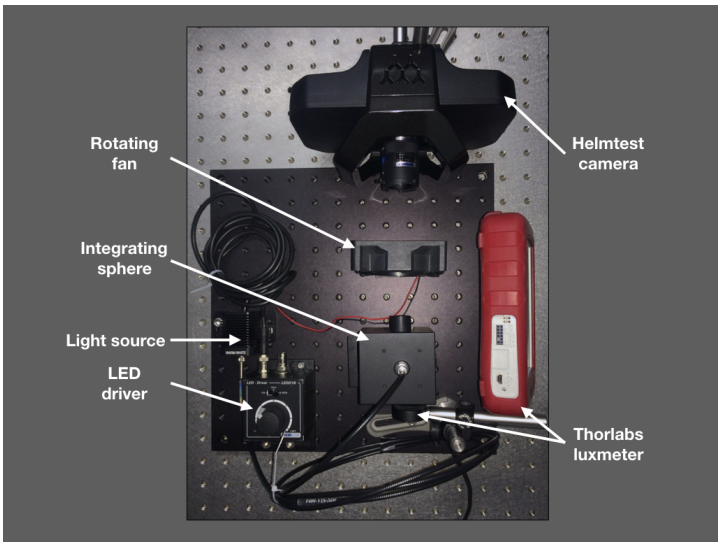

Figure 33: Setup used to compute the optical flow on a rotating fan under a low illumination. The output of the integrating sphere is monitored with a Thorlabs power-meter.

more complete on the recording with the cooling system on. We now measure both the norm and angle of the optical flow at the upper edge of the blade for a range of 275 RPM to 1730 RPM. Results are shown on Fig.34 and Fig.35.

The yellow data correspond to the reference value for the norm and angle of the optical flow. The dark red data correspond to the recordings without the cooling system, and the dark blue data with the cooling system activated. Beyond 625 RPM and without the cooling system, the signal is too weak. Moreover, unlike for the angle value, the norm of the optical flow is underestimated when no cooling is activated. Once the Peltier coolers are on, the SNR increases and the measure of the optical flow is improved. Above 1730 RPM the norm of the optical flow overshoots and diverts from the ground-truth. At this rate, the number of events used to compute the flow is drastically reduced, and as expected we lose precision. However, we gained a factor 3 in the detection sensitivity by merely cooling down the sensor.

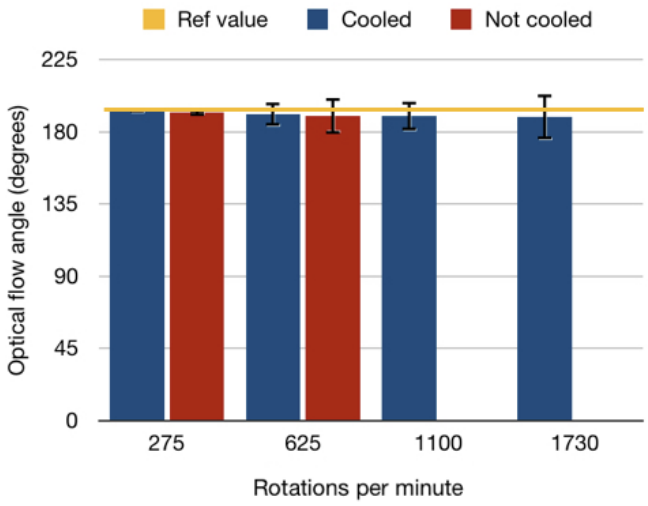

Figure 34: Measure of the angle of the optical flow vector for different rotating speeds. The dark blue data are results with the cooling system and the dark red ones without. The yellow line corresponds to the reference value.

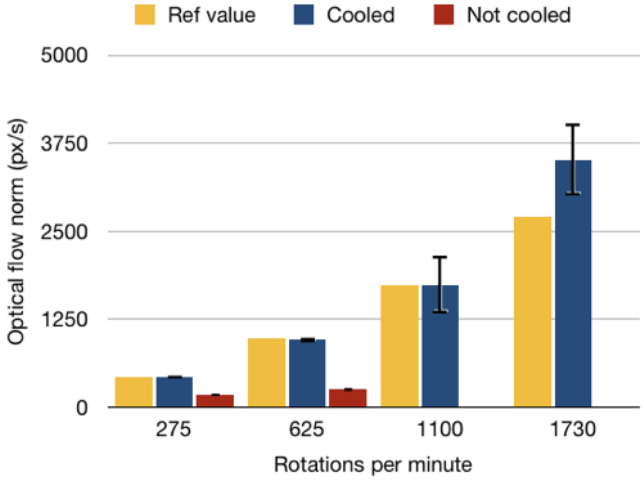

Figure 35: Computation of the norm of the optical flow with (dark blue) and without (dark red) the cooling system. The yellow data correspond to the reference value.

Additional experiments show that results are consistent on other regions of the optical flow map.

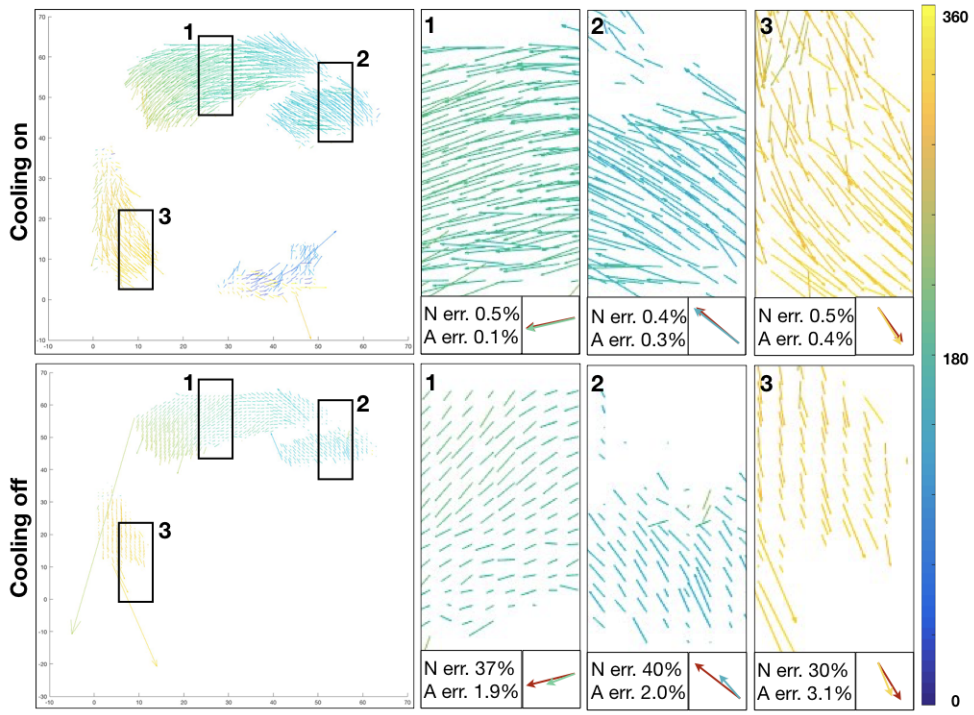

Figure 36: Representation of the fan's optical flow at 275 RPM with both the cooling system on (top section) and off (bottom section). Areas 1, 2 and 3 are three zooms with at the bottom the mean optical flow for the widow, superimposed with the ground-truth in red. The colors correspond to the angle of the optical flow, from dark blue for 0 degrees to yellow for 360 degrees. N err. is the error of the norm from the ground-truth and A err. the error on the angle of the flow.

Let us now look at the effect of cooling the sensor on another application geared toward microscopy. We use for that a reflection based microscope to observe small particles floating in water. Flow is induced inside a microfluidic chip with a syringe as shown on Figure.37. We tune the light power to be 2 lux at the sensor plane and use an event-based blob tracking algorithm similar to the one described in [27]. Any object moving in the field of view generates a cloud of events that can be represented by a bivariate normal distribution, in other words a blob, that updates its position with each new event. Each micro-particle is assigned with a blob tracker (in green on Figure.38), provided that enough events are generated. This enables us to track and count the number of particles $N_{particule}$ that cross the field of view. For that, we increment a counter when the center of a tracker crosses a virtual line (in red on Figure.38).

We can fine-tune the parameters of the algorithm in order to associate a tracker when very few events are generated, however we become very sensitive to noise. Indeed many trackers are falsely cre-

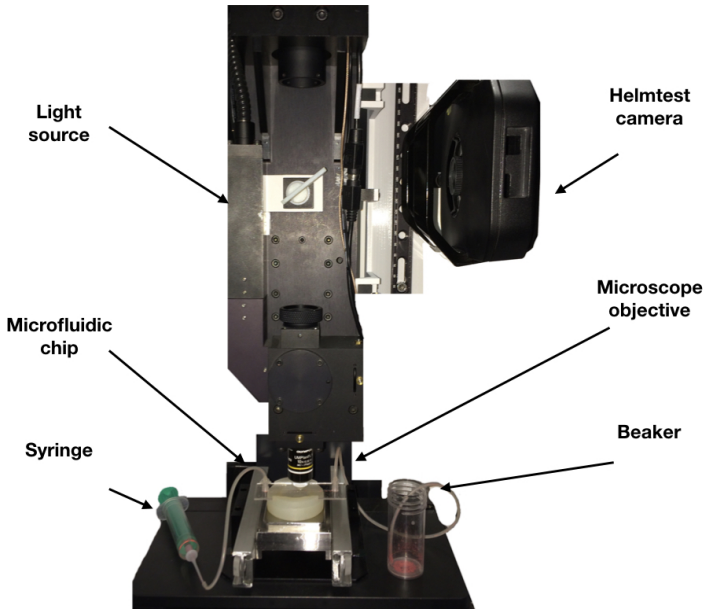

Figure 37: Event probability vs. stimulus contrast for a low level of light.

ated due to noise events, and the number of actual particles is over-estimated. This limitation sets the lower boundary for the fine tuning of the algorithm. As a result, for high particle velocities and without the cooling system, no trackers are generated, and we miss objects that cross the field of view. Results are shown on Table.2 for a slow velocity (flow of 3ml/h), a medium velocity (flow of 9ml/h) and a high velocity (flow of 15ml/h).

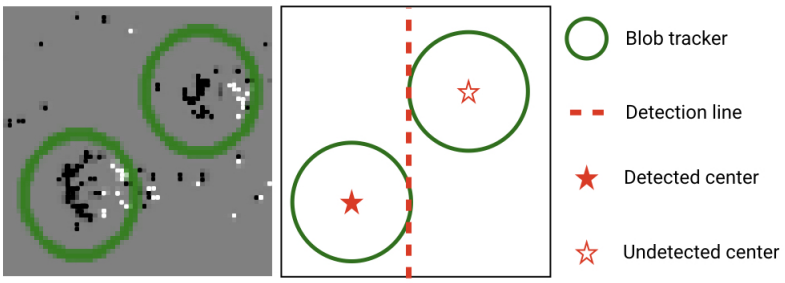

Figure 38: Event probability vs. stimulus contrast for a low level of light.

Table 2: Effect of the cooling system on particle counting

	Slow		Medium		Fast	
	Hot	Cold	Hot	Cold	Hot	Cold
$N_{particule}$	250	243	430	802	320	1040
Error	3%	4%	43%	8%	75%	17%

When the cooling system is activated, the noise is reduced. Particles are not generating more events, but we can lower the number of minimum events to create a tracker without being noise polluted. Counting particles flowing with higher velocities is now possible.

3.4 DISCUSSION AND FURTHER IMPROVEMENTS

It was a crucial step to work on a new version of the sensor which does not require high levels of light in order to perform well. Indeed, such an illuminance cannot always be reached especially in microscopy and biology where side effects such as photo-bleaching must be avoided. The Helmtest event-based camera we presented here shows a significant improvement in low light conditions and with low contrast variations. That makes it a potential candidate for any medical imaging device with a low light input source, like for instance reflection based microscopes. We showed with a computation of the optical flow and with the use of a tracking algorithm that cooling the sensor also significantly increases our detection capacity.

However a full calibration of a camera would require more extensive work. Indeed, the results presented here have been obtained with a given set of parameters which were of interest for this thesis. In particular, the camera's internal electrical components are tuned via a set of analogical values called "bias". They correspond to a set of voltage values that set the physical limits of the electronics. Depending on their values, properties of the pixels such as the detection threshold, the latency, the refractory period and many others may change. For our experiments, we have been working with a fixed set of bias with the hypothesis that the camera's parameters would remain unchanged when the temperature fluctuates. In order to gain in accuracy, a measure of those parameters with and without the cooling system activated would be necessary.

To sum up, thermal noise can be reduced with a cooling system in event-based sensors. The version we designed showed an increase of the SNR when the chip was cooled down which enabled a finer tuning of the algorithms. Yet, this camera remains a university project and as such is limited compared to firm made devices. The pixel pitch, for instance, is quite large compared to the state of the art asynchronous sensors. This limits the observation of small structures. The handheld microcirculation device, which will presented in the next chapter, has a magnification of $\times 20$ and a minimum pixel pitch of $30\mu m$ is necessary.

4

PROTOTYPE FOR MICRO-CIRCULATION IMAGING

The use of a bulky microscope such as a FFOCT device is not a viable solution for day-to-day monitoring of the micro-circulation. We have used this methodology to develop a first proof of concept, yet we now need to move on to a more compact system for our target application: observing the microcirculation at the patient's bedside. Twenty years ago, Groner et al. introduced Orthogonal Polarization Spectral (OPS) imaging, allowing the development of a hand-held microscope to study blood capillaries [19]. This opened new perspectives in the field of micro-circulation study in care facilities, especially regarding the monitoring of diseases and therapy during surgery. Moreover, several studies have shown the benefits of sub-lingual micro-circulation monitoring during sepsis, shock and resuscitation [57, 69]. It was shown that the blood flow is mainly altered within the smallest capillaries, making their study of the utmost importance [34].

The principle of OPS imaging relies on the polarized illumination of a biological sample. The back-scattered light goes through an analyzer (polarizer orthogonal to the polarization of the incident light) before being captured by the camera. Any direct reflection is therefore filtered as the polarization state is not altered. On the opposite, the light that has been diffracted by the sample gets depolarized and passes through the analyzer. This process allows the observation of subsurface structures.

The main drawback of this method is the significant attenuation of light power due to the analyzer which cuts of most of the signal. The weak amount of light captured by the camera makes this imaging technique more subject to motion blur induced by the movements of the device, of the tissues and of the flow of red blood cells. In larger vessels, the granular aspect of the blood flow is harder to observe making it increasingly difficult to estimate accurate velocities.

In the light of these limitations, a novel imaging modality known as Sidestream Dark Field (SDF) imaging was developed by Goeghart et al. in order to study sub-lingual micro-circulation [18]. We used this imaging modality to develop our hand-held micro-circulation device. The target is to develop a complete setup accessible at the patient's bedside which can be operated by any professional from the medical world [63].

4.1 SIDESTREAM DARK FIELD MICROSCOPY

In SDF imaging, the incident light forms a ring-shape around the area of interest. LEDs are arranged in a circle all around the optical system and shine on the outer boundaries of the region of interest as seen on Figure.39. The light will diffuse inside tissues and illuminate the sample thanks to the principle of diffraction. In this respect, the lenses that capture light back-scattered by the biological sample are isolated from any specular (mirror-like) reflection.

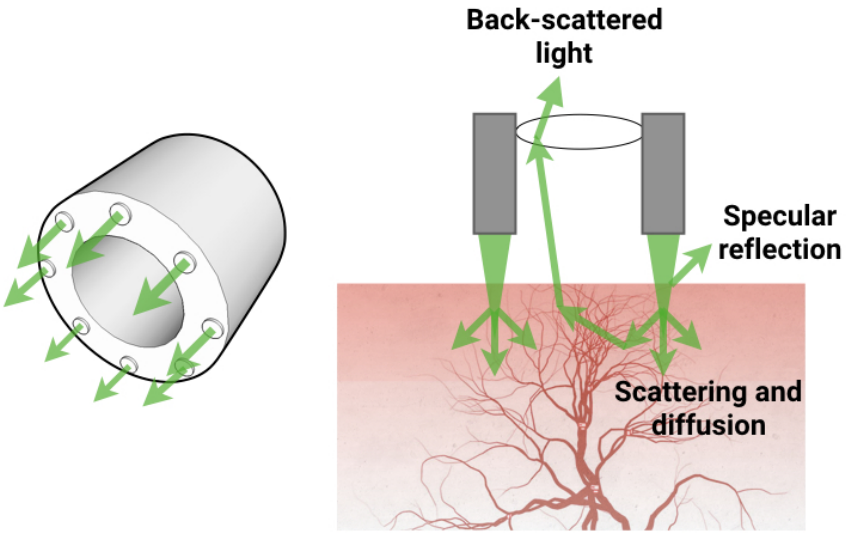

Figure 39: Principle of Sidestream Dark Field imaging. Left: Ring-shaped light source. Right: Principle of illumination on a biological sample. Light diffuses inside the tissues and is back-scattered to the camera.

The LEDs emit at a central wavelength of 530nm. This ensures a sufficient optical absorption by the (de)oxyhemoglobin-containing red blood cells in contrast with the rest of the tissue embedding the micro-circulation. This creates contrast as the RBCs appear darker than the background.

4.2 OPTICAL SETUP

The optical setup used in our device is based on the conventional reflection-based optical microscope scheme. Its development was partly done by Christophe Leroy-Dos Santos for the illumination part of the system as well as the 3D design of the casing. The sample is illuminated by three LEDs emitting at a central wavelength of 530nm. A bundle of 24 optical fibers (in green on Figure.40) are arranged in a circle in a similar fashion as what is shown on Figure.39. This pro-

vides a ring-shape illumination on the tissues. To ensure maximum throughput of light, an elliptic mirror (in gray on Figure.40) is embedded in the terminal part of the micro-circulation device. Its role is to focus a maximum of light rays onto the sample.

The optical alignment that captures the back-scattered light is composed of the following components:

- A glass cover sapphire window located at the object plane and represented in purple on Figure.40. This window will be placed directly in contact with the tissues and separates the sample from the rest of the optical system.
- A molded aspheric lens of focal length 5mm, represented in blue on Figure.40.This lens acts as the *objective-lens* in a conventional optical microscope scheme. Its numerical aperture is 0.15 and has an anti-reflective coated.
- An achromatic lens of focal length 100mm, represented in orange on Figure.40. This lens is our *eyepiece-lens* and will create an image at the sensor plane.
- A Varioptic liquid lens that enables auto-focusing, represented in yellow on Figure.40. The working principle, as well as focusing properties of this component, will be further detailed in the next chapter.

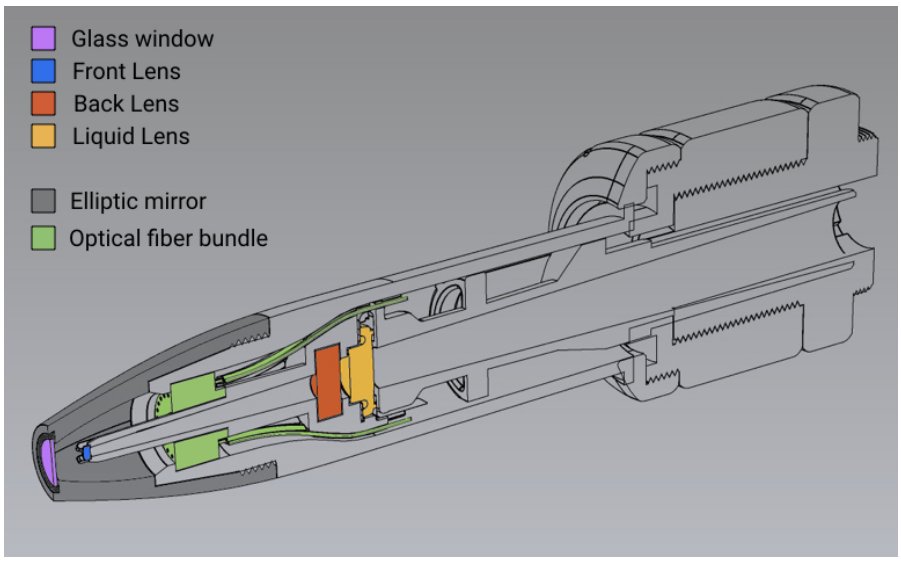

Figure 40: Drawing of the micro-circulation device with its optical setup. In green is the bundle of optical fibers. In gray is the elliptic mirror that ensures a proper annular illumination. In purple is the cover glass window. In blue is the *objective lens*. In red is the *eyepiece lens*. In yellow is the liquid lens.

The optical system was initially designed with Zemax in order to evaluate its performances in term of spatial resolution, aberrations and estimate other physical properties such as the zoom. Both models for the lenses and the glass window were provided by the manufacturing company, and we approximated the liquid lens by two liquids enclosed between two cover windows. The two liquids are immiscible and have different refractive index n. The first one is a non-polar hydrophobic oil for which $n_{oil} = 1.477$ and the second is a polar water solution for which $n_{water} = 1.388$. The optical indexes of all the components were provided by Varioptic. In the real model, both liquids have the same density in order to avoid any deformation of the meniscus due to the gravity. More details on the working principle of the liquid lens will be given in the next chapter. The total magnification is $\times 20$.

We will now have a look at several parameters to characterize our optical system:

- The Point Spread Function (PSF) : it is the irradiance distribution that results from a single point source in object space. The PSF gives an estimate of the spatial resolution of a system.
- The Geometric Encircled Energy (GEE) : it corresponds to the light power distribution when moving away from the focus point.
- The Optical Path Difference (OPD) Fan and the Ray Aberration Fan : OPD is a plot of the optical path difference as a function of the pupil coordinate, and Ray fan is a plot of the aberrations as a function of the pupil coordinate.

In the real world, although an object is a point, its image formed through an optical system is never a point as well. The two reasons for this are firstly the aberrations of the system which spread the image on a finite area and secondly the diffraction effects which also spread the image. Our setup is not diffraction limited, meaning that the image of a point is larger than the Airy disk reference that would be formed by an ideal aberration-free system. Here, mainly the aberrations are responsible for the formation of the image. We therefore compute the geometric PSF: many rays from a single point source in object space are launched, go through the system and finally the (x,y) coordinates of all the relative rays are plotted. On Figure.41 is shown the PSF for two points in the object space. The first one is on the optical axis, the second is off-axis, $0.13mm$ away both on the x and y axis, which corresponds to the limit of our field of view.

On the optical axis, we see that the geometrical radius is $16.1\mu m$ meaning that an object point will roughly give a point as an image

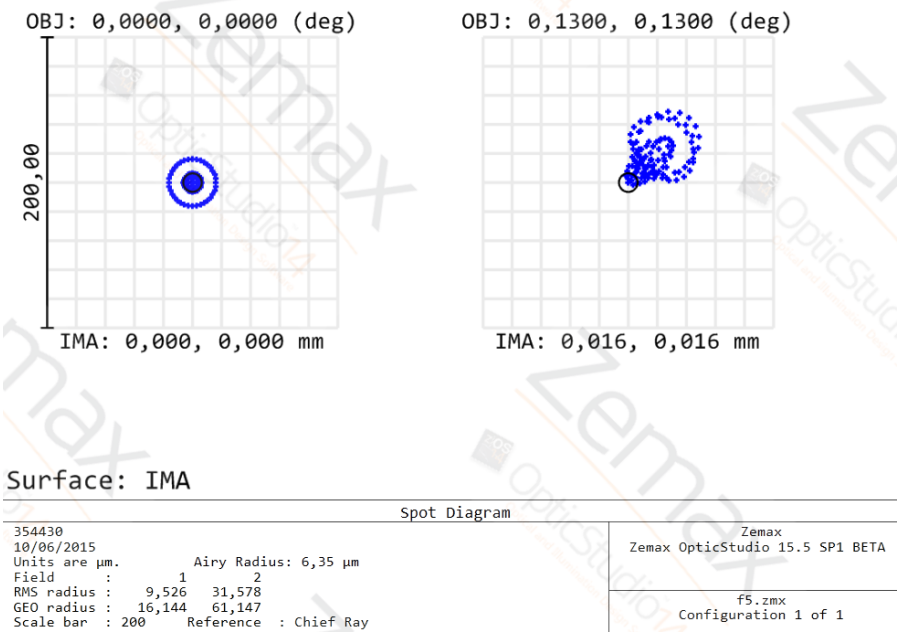

Figure 41: Point Spread Function of two object points: on the left is a point on the optical axis, on the right is an object 0.13mm along the x and y axis. The system is not diffraction limited as the PSF is larger than the Airy disk (black circle).

(the pixel pitch is 11µm). At the edges of the field of view, the geometrical radius increases to 61.1µm, and a blurry spot will be formed. Small structures will be harder to image the further we move away from the optical axis.

The GEE is shown on Figure.42. The blue curve is for the object on the optical axis and the green curve for the object off-axis. For the object on axis, 70% of the light power will be focused on a single pixel and 95% of the energy will be contained within the direct neighbor pixels. For an object off axis, the total light power will be distributed over a region of 5×5 pixels. This result is in line with the PSF shown in the previous section.

The OPD fan is a plot in both the x and y directions of the optical path difference as a function of the pupil coordinate. In a perfect optical system, the optical path of the wavefront is identical to that of an aberration-free spherical wavefront in the exit pupil. The OPD fan for our system is shown on Figure.43.

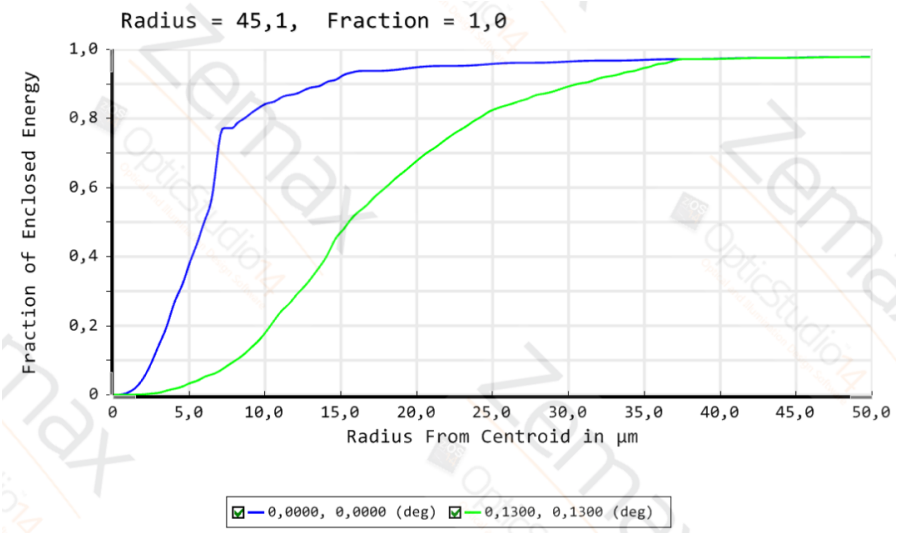

Figure 42: Fraction of enclosed energy with respect to the radius from the centroid. The blue curves correspond to the image on the optical axis and the green curve to the image off axis.

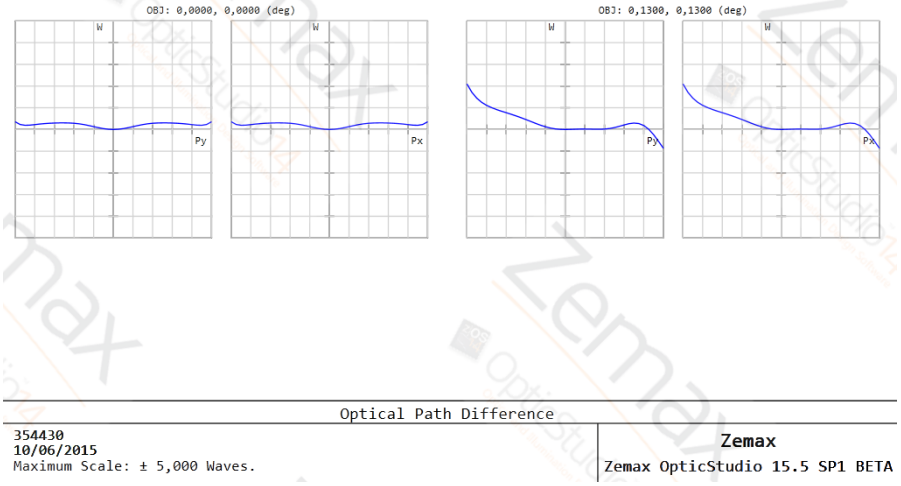

Figure 43: Optical path difference: on the left, on axis, and on the right, off axis.

Let us finally look at the ray fan. Generally, when a ray passes through the optical system, its point of intersection in the image field falls on some small but nonzero distance away from the chief ray. Once again, in a perfect optical system, the ray aberrations should be zero across the pupil. We show on Figure.44 the ray fan for an object on axis and an object off axis.

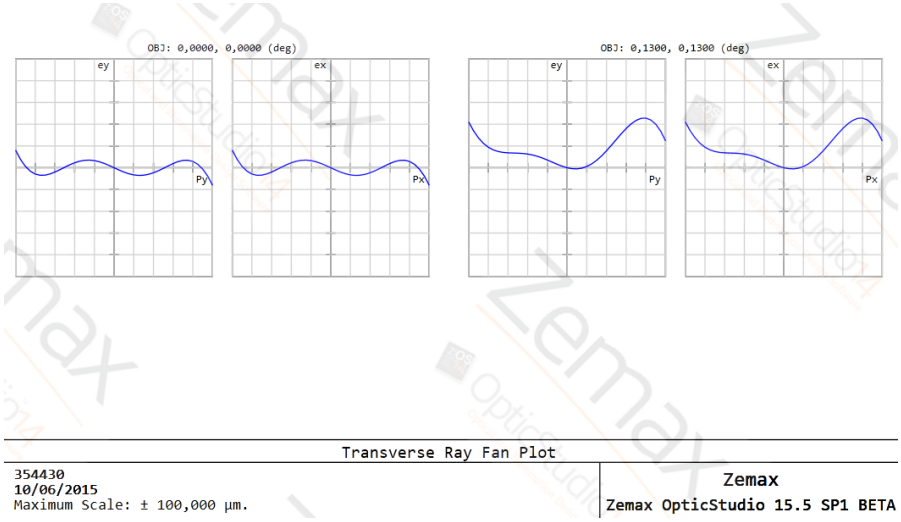

Figure 44: Ray fan: on the left on axis and on the right off axis.

When fully assembled with the event-based camera, the system looks like on Figure.45 and Figure.46.

Figure 45: Micro-circulation prototype for sub-lingual capillaries imaging.

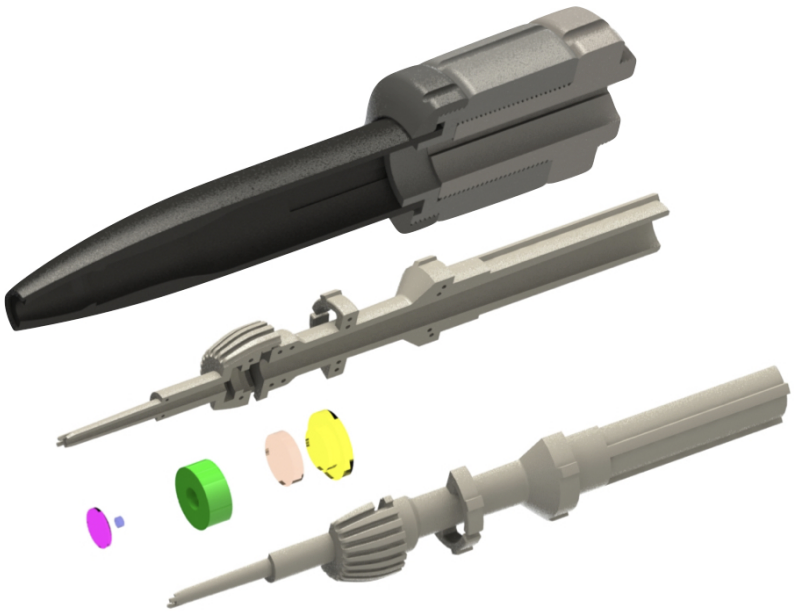

Figure 46: Exploded view of the micro-circulation prototype for sub-lingual capillaries imaging. The colors of the optical components are the following: purple for the glass window, blue for the objective lens, green for the optical fiber bundle, orange for the eyepiece lens and yellow for the liquid lens.

4.3 AUTOFOCUS WITH THE LIQUID LENS

The liquid lens previously described in this chapter helps to reduce defocus. Defocus is the principal optical aberration in our optical setup when looking at capillaries located at different depths. Indeed, blood capillaries inside the mouth are located within the first few hundred microns of the tissues' mucous membrane. Depending on the region of interest, our system needs to adjust itself to the proper imaging depth in order to have a sharp image.
There are two methods to tune the focus: either change the focal length or the distance between the camera and the object. Here we use a tunable liquid lens as moving the camera would create motion artifacts. Based on collaborative work with G. Haessig in "*A Spiking Neural Network Model of Depth from Defocus for Event-based Neuromorphic Vision*" which is currently pending publication, we adapted the algorithm to perform auto-focus. The principle relies on the assumption that sharpness is reached when the size of the blur spot is minimal. The advantage of our method lies in the simplicity of the focus detection, while conventional frame recording methods use focus detection algorithms based on auto-correlation or convolution such as Log-histogram, variance or energy of the image [48, 70, 74].

When an object is located before or after the focus point, it will form a blurry image of size s. Geometrical optic relations (Figure 47) give :

$$s = \frac{f^2}{N} \times \frac{|z-d|}{(d-f)z} \tag{19}$$

with N the numerical aperture of the system, f the focal length, d the position of the point in focus and z the position of the object. N is defined as the ratio of the focal length divided by the aperture of the system.

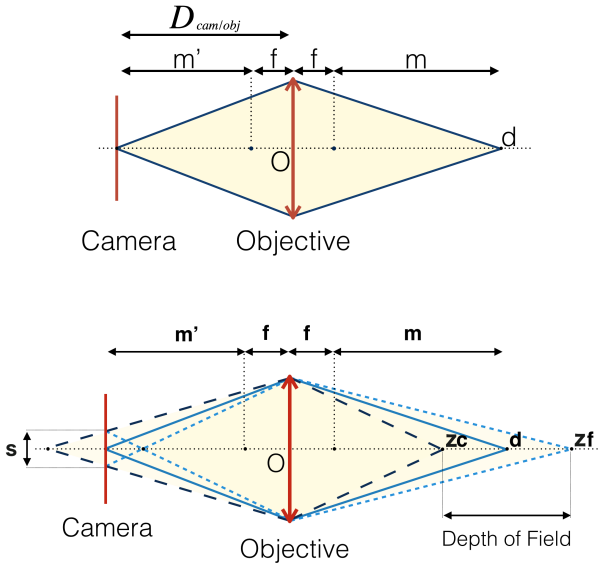

Figure 47: Top: Stigmatic optical system. Bottom: Principle of depth from defocus.

A real optical system has a finite aperture size, limited by the dimensions of the optics. The spatial resolution is also limited by the pixel size below which it is not possible to distinguish focus. This represents the circle of confusion, C, of the camera as shown on Figure 47. As a consequence, a range of several points will form an image "in focus" (the image spot size is smaller than the circle of confusion) on the detector for a given focal length. This range is called depth of field, and the two limiting points are the values of z_{close} and z_{far} for which $s = C$, i.e.

$$z_{close/far} = \frac{d}{1 \pm \frac{CN(d-f)}{f^2}} \tag{20}$$

The depth of field is then given by computing the difference between z_{close} and z_{far}:

$$D_oF = |zf - zc| = 2 \times \frac{CNd(d-f)}{f^2 - \frac{(CN(d-f))^2}{f^2}} \tag{21}$$

The size of the blur spot of an out of focus object grows with the distance respectively to the depth of field (DoF) zone. In other words, when the object is in focus, the image spot will have its minimum size and the contrast will be maximum (sharp edges). When we sweep the focal length of the liquid lens over its dynamic range, objects will successively appear out of focus, then in focus and out of focus again. The blurry spot around the object will therefore shrink until the object is sharp and grow again. Our aim is here to stop when the object is precisely in focus.

We study the size modification of a blur spot when an object is in or out of focus. Let us consider a small luminous object that will successively be out of focus, in focus and out of focus again. We record over time local changes of the luminance as shown on Figure 48. The size $s(t)$ of the defocus blur at the sensor plane will vary according to the equation 19. Due to the aberrations, diffraction phenomenon and non-idealities of the lenses, a Gaussian point spread function is commonly used to describe the defocus blur spot [37]. The spread parameter $\sigma(t)$ is proportional to the diameter $s(t)$ of the ideal blur circle, i.e. $\sigma(t) = \alpha s(t)$. The resulting intensity onto the sensor, at a pixel (x_i, y_i) is:

$$I_{i,j}(x, y, t) = A.\exp\left(-\frac{r_i^2}{2\sigma(t)^2}\right). \tag{22}$$

with $r_i^2 = (x - x_i)^2 + (y - y_i)^2$ and A the amplitude. At the pixel level the evolution of the intensity will depend on how close to the object it is located. As a function of time, the standard deviation in I can be used to determine the time t at which an event is triggered by the pixel, assuming σ is invertible i.e.:

$$t = \sigma^{-1}\left(\sqrt{\frac{r_i^2}{2\left(\log A - \log I_{i,j}(x, y, t)\right)}}\right) \tag{23}$$

We are dropping subscripts (i, j) for readability purpose as what we are describing is true for any pixel in the sensor. Hence, given the intensity at an arbitrary time t_0, if the variations of its log reach some threshold $\pm n$, then:

$$\log\frac{I(x, y, t)}{I(x, y, t_0)} = \pm n \text{ and } \log I(x, y, t) = \log I(x, y, t_0) \pm n. \tag{24}$$

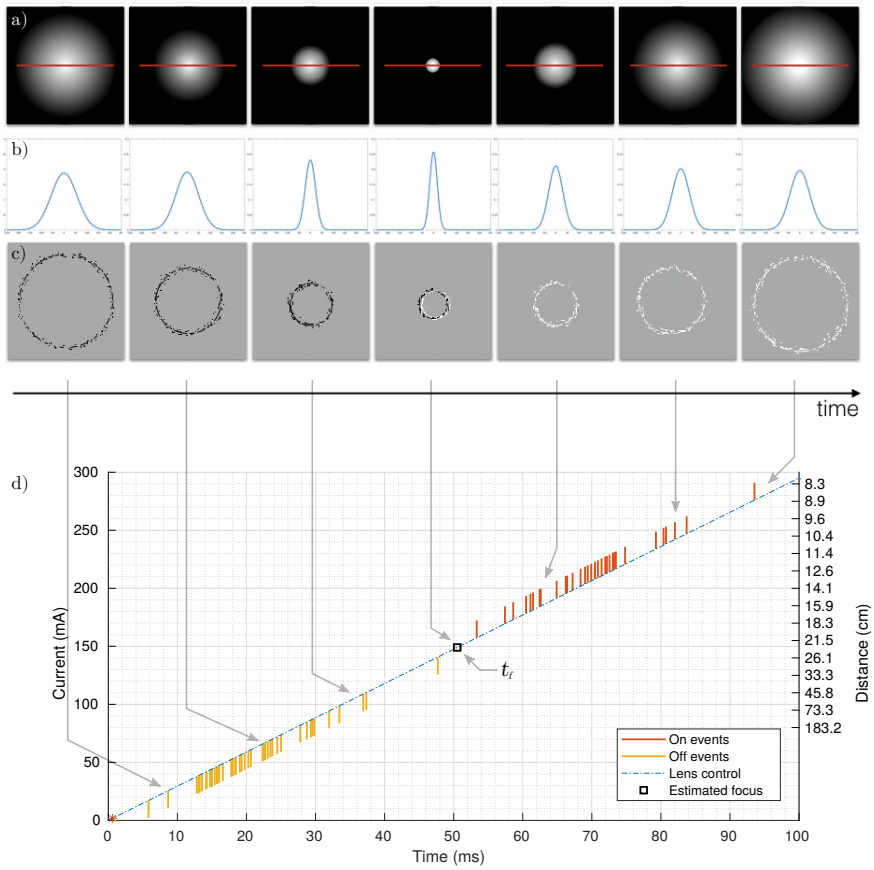

Figure 48: (a) Successive snapshots of a sphere when sweeping the focus range. The red line represents a line of pixels in the y-direction. (b) Variations of the intensity profile along the red y-axis on the above snapshots. (c) Events corresponding to the sweeping of the focus range, in black are OFF events and in white ON events. (d) Representation of spikes among a single pixel, according to the driving current of the liquid lens. Here, the focus point is estimated to be at 22.6cm from the sensor.

This gives the time when an event is emitted according to (23):

$$t = \sigma^{-1}\left(\sqrt{\frac{r^2}{2(\log A - \log I_0 \mp n)}}\right) \tag{25}$$

The sign of n is chosen according to the polarity of the spiking event, itself related to the sign of the intensity's derivative:

$$\text{SIGN}(n) = \text{SIGN}(p) = \text{SIGN}\left(\frac{dI}{dt}\right) \tag{26}$$

When the derivative is positive the polarity will be +1 (ON event) and -1 when negative (OFF event). (25) is telling us when an event

will be emitted w.r.t. n and to a reference event measured at t_0. As we reach focus, the value of σ will be constant for small duration of time, therefore the derivative of I, $\frac{dI}{dt}$ is equal to 0, followed by a polarity change as shown in Fig.48(c) and expressed in the temporal domain in Fig.48(d) around 50ms. The detection of focus can then be determined by detecting the time t_f of the polarity change that can be estimated from the average timing between the consecutive ON and OFF events.

We now know the exact time of focus which corresponds to a fixed value for the focal length of the liquid lens.

We use in our system a focus-tunable liquid lens with a 3.9 mm clear aperture and focus range of −5 to 15 mm. The electrically controllable lens has an electromagnetic actuator which changes the shape of the lens, resulting in a change of the focal length as shown on Figure.49. The physical principle relies on the modification of the surface tension of the enclosed liquids, depending on the amplitude of the voltage applied.

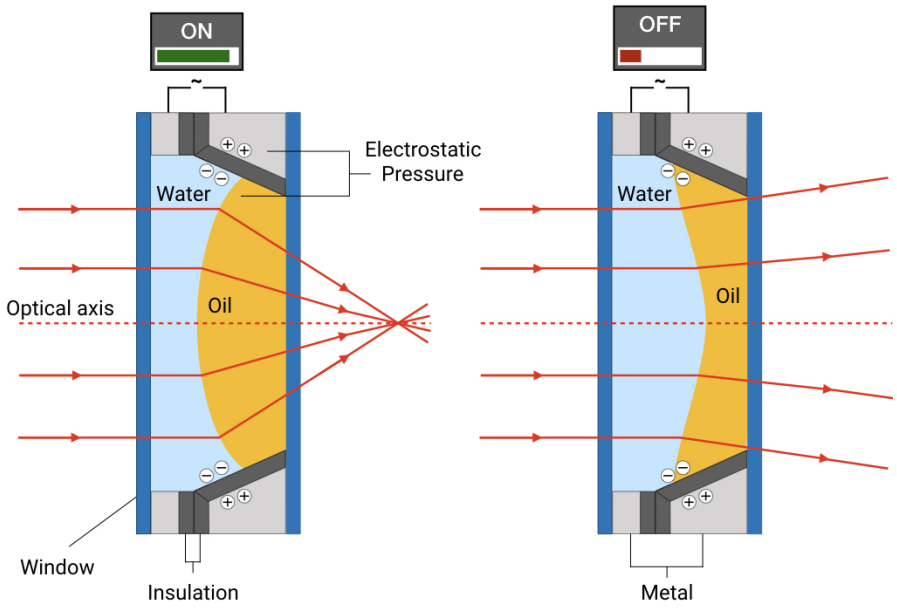

Figure 49: Working principle of the liquid lens. The voltage difference induced by the actuator forces the shape of the water/oil diopter to change.

The actuator is current controlled, designed such as the focal length f_{ll} is inversely proportional to the current:

$$Ic(t) = \gamma / f_{ll}(t), \tag{27}$$

with γ fixed. We control the lens with a triangular signal $Ic(t)$ and since we know the time of focus t_f we can get back to the value of the current and set the proper focal length to be in focus.

We test our method by searching the optimal focus when observing blood capillaries inside the mouth. We use the event-based sensor to perform auto-focus with the methodology previously described and verify the improvement by using a conventional frame-based camera (IDS sensor). Results are shown on Figure.50.

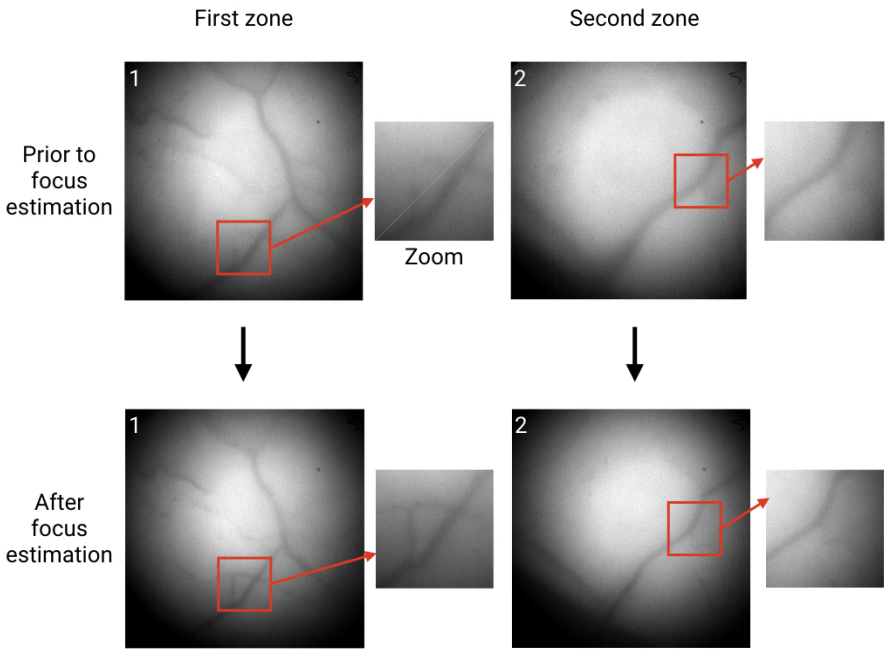

Figure 50: Results of the auto-focus algorithm. The top pictures are taken before tuning of the liquid-lens and the bottom pictures show the same region of interest after auto-focus.

SUMMARY

Apart from defocus, which is compensated for with the liquid lens, the aberrations in our system are the following: spherical, coma and field curvature. The spherical aberration is minimal and will not affect our recordings. Both coma and field curvature will result in a degradation of the signal the further away we are from the optical axis. In order to continue reducing the aberrations, it would be necessary to replace a lens with a strong radius of curvature (for instance the front lens) with two lenses. However, this will make the system more complex and more expensive.

We also presented in this section a method to perform auto-focus with an event-based camera and a liquid lens. The aim is to mini-

mize the defocus optical aberration in the micro-circulation device we designed. It is difficult to assess the performances of such an algorithm, and we encountered difficulties in reaching what we think is the "best" focus with this technique. However, this method is fast and computationally inexpensive. It can easily be adapted on embedded electronics such as a FPGA or even directly on chip (see "*A Spiking Neural Network Model of Depth from Defocus for Event-based Neuromorphic Vision*" for more details).

We have been focused on hardware development in this chapter with both a work on a low light event-based camera and the design of a portable micro-circulation device. From our initial proof of concept with the event-based/FFOCT association, we are moving one step closer towards studying red blood cells in-vivo. In the last chapter of this thesis, we will focus on the type of data we can extract from micro hemodynamics with an event based sensor. More precisely we will determine the following dynamic morphological parameters: micro-circulatory blood flow velocity and blood cell concentration. This work was done in parallel to the hardware development we presented here. Therefore the results in the next section have been obtained with a full-size microscope version of our system.

Part III

IN-VIVO ANALYSIS OF HEMODYNAMICS

5

TOWARDS IN-VIVO RED BLOOD CELL IMAGING WITH AN EVENT-BASED SENSOR

We stated previously that the Helmtest camera presented in chapter 4 is limited by its pixel size. In parallel to its development, Prophesee has been working on a new version of the ATIS camera, shown on Figure.51, with a VGA sensor. It benefits from a smaller pixel pitch, $11 \times 11\mu m$, an increased fill factor of 60%, an array of 640×480 pixels. We will use this camera for the remaining of this thesis.

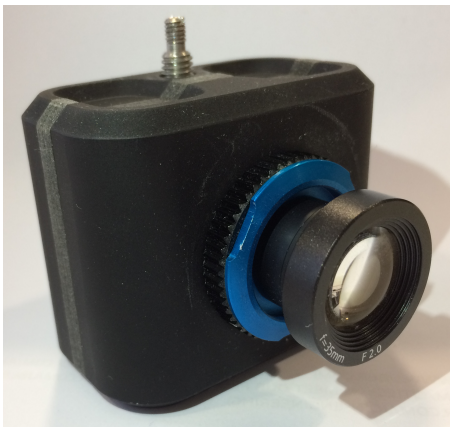

Figure 51: Sisley VGA asynchronous sensor developed by Prophesee.

In a first instance, we will study the micro-circulation on a mouse's cremaster muscle (thin layer of striated muscle surrounding the testis) using a microscope. Our aim is to estimate microhemodynamic parameters with the event-based sensor.

5.1 SURGICAL PROCEDURE

The experiments of this chapter were performed at the Laboratoire d'étude de la microcirculation (Microcirculation, Biogénergétique, Inflammation et insuffisance circulatoire aiguë, U942, Université Paris Diderot, 10 avenue de Verdun, Paris, France). We used male mice weighing approximately 20g. The animals were fed standard mouse diet and had free access to water. The observation of venules was conducted on a microscope (Leitz, Germany) with a saline immersion objective ($\times$25, Leitz, Germany). Experiments were recorded with HCImage software (Hamamatsu Photonics, Japan) connected to a digital camera Hamamatsu (C11440) together with the Sisley sensor. The Hamamatsu camera will serve as ground-truth in our experiments.

Induction of anesthesia was performed similarly to the technique described in [45], with isoflurane (1.5–2%) followed by an intraperitoneal injection of ketamine (150mg/kg), xylazine hydrochloride (5mg/kg) and atropine (1mg/kg). Anesthesia was maintained throughout the experiment with additional injections of the same drug preparation (a quarter of the initial dose).

The pedal withdrawal reflex was tested every ten minutes by pinching the foot pad. If the animal withdrew his leg in response to the foot pad stimulation, then a dose was administered. Animals were lying on a heating blanket (temperature 38°C) in supine position.

A tracheotomy was performed, and a cannula was inserted into the trachea to facilitate spontaneous breathing. The right carotid artery was catheterized with a PE-10 polyethylene cannula. This catheter was filled with 0.9% saline and connected to a pressure transducer (MP30, BIOPAC systems) for continuous recording of systemic arterial blood pressure (MAP).

The left cremaster muscle was prepared according to the technique described in [3, 4]. Briefly, the muscle was detached from the scrotum. A transverse buttonhole slit about 5 mm long was made in the proximal part of the cremaster pouch. The testicle, epididymis, and the cremaster itself were then drawn out through the buttonhole. This procedure led to the invagination of the cremaster, which acquired a finger shape, with the cremaster pouch now turned inside out. The small pedicle that attaches the cremaster to the testicle was tied up with two stitches and cut between them, to separate the cremaster completely from the testicle. A flexible extensible ovoid ring was made with metal wire (diameter, 0.1 mm) and expanded gently, spreading out the cremaster that acquired a racket shape. The ring was positioned so that the main cremaster artery was in the center of the racket's upper surface. Throughout these procedures, the muscle was continuously bathed with saline solution. This procedure involves minimal incision of the cremaster and so reduces considerably the risk of hemorrhage and lesions of both the muscle and its micro-circulation. Because the size of the ring is adapted to the dimensions of the cremaster, the extension of the muscle is sufficient to allow good optical resolution, but does not affect the micro-circulation. The muscle preparation was covered with transparent film and continuously superfused (2mL/min) with Krebs solution (in $mmol.L^{-1}$, NaCl 118, KCl 5.9, $MgSO_4$ 0.5, NaH_2CO_3 28, $CaCl_2$ 1.25, glucose 10) warmed at 34.5°C and bubbled with gas mixture (O_2 0%/CO_2 5%/N_2 95%) throughout the experiment.

5.2 ACTIVITY OF BLOOD VESSELS

The first parameters we evaluate are the absolute and relative perfusions of blood vessels. We define the activity A_{rbc} of a capillary as its number of erythrocytes per $100\mu m^2$ each ms. We assume that individual red blood cells can be associated with a mean number of events N_{rbc} that depends on the magnification of the microscope objective and the imaging modality (fluorescence imaging, transmission or reflection microscopy, etc.). Let N_{cap} be the total number of events per $100\mu m^2$ each ms within a capillary. The activity is computed as follow:

$$A_{rbc} = \frac{N_{cap}}{N_{rbc}} \tag{28}$$

From the estimation of this activity we produce two types of outputs that will be further detailed in the next two sections:

- An absolute activity map.
- A relative activity map.

In a first instance we will focus on the absolute perfusion map which corresponds to the local activity of capillaries within the field of view, i.e. the number of red blood cells that flow in the network of vessels. This output gives an estimate of how well capillaries are perfused and the red blood cell distribution.

We first create a binary mask that corresponds to the shape of the vessels network. This mask is computed using the sum of the incoming events generated by the camera during a short period of time. The zones with the most events correspond to the areas with the most significant contrast variations and therefore to the location of the vessels. An adaptive threshold is used to generate the binary mask depending on the maximum activity recorded during this time window. The binary mask is then divided into smaller regions as seen on Fig.52 thanks to a series of morphological operations.

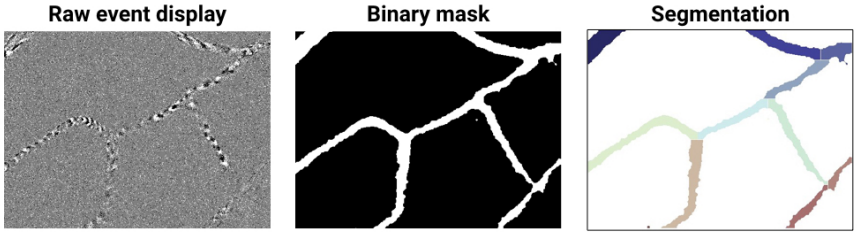

Figure 52: Computations steps from left to right: Event reconstruction on a time window of 100ms, Binary mask corresponding to the capillaries' network and corresponding segmentation.

For each incoming event, the activity of the associated region is updated. The segmentation step allows a global averaging on a greater

set of events within a capillary branch and therefore a more accurate estimation of the activity. The absolute perfusion map provides the activity of a vessel in RBC per $100\mu m^2$. We compared our results to a baseline recording from a Hamamatsu camera *ORCA Flash 4.0* as seen on Figure.53. This camera has a 2048×2048 pixel resolution and provides 30 frames/s at full resolution and up to 25 000 frames/s with the lowest resolution.

Figure 53: ORCA Flash 4.0 Hamamatsu camera.

On Figure.54 is shown both the baseline from the Hamamatsu camera on the left and the absolute perfusion map computed from the event-based data on the right. Results are displayed in number of red blood cells per $100\mu m^2$. In order to compare our estimations with a frame-based acquisition value, we counted manually on the output videos from the Hamamatsu, the number of red blood cells within three different regions 1, 2 and 3. The recording lasted 1mn each and cell were counted in the selected regions every 50 frames (120 frames in total) and averaged. Results are shown on Table.3.

SQUARE	EVENT-BASED	FRAME-BASED
zone 1	2.0	2.2
zone 2	2.4	2.8
zone 3	3.6	4.0

Table 3: Erythrocytes density estimation: number of RBC for $100\mu m^2$.

In small capillaries such as regions 1 and 2, individual red blood cells are lined up in a single file and touch one another. The diameter of a cell in approximately $7\mu m$ which corresponds roughly to a surface area of $50\mu m^2$. We expect the density of erythrocyte to be around 2 cells per $100\mu m^2$. Both results from the frame-based baseline and the event-based computation are close to this value. In a larger capillary such as region 3, estimating the number of red blood cells is

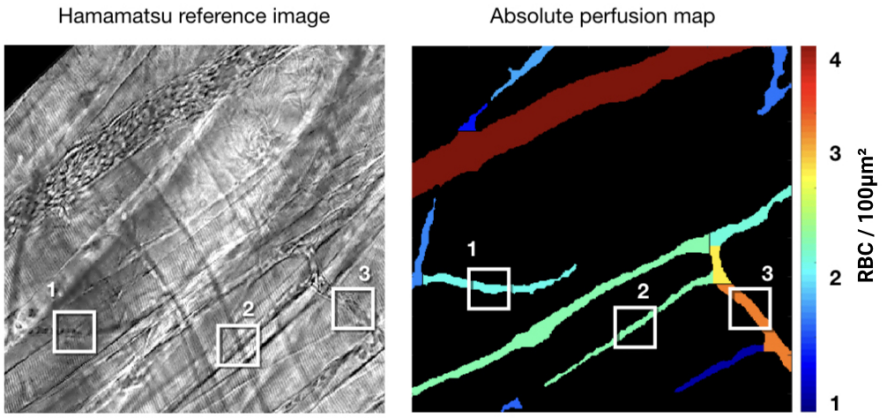

Figure 54: Right: Gray level image from a Hamamatsu recording at 100 frames per second. Left: Absolute perfusion estimation using the event-based data.The three white squares correspond to the regions where the red blood cells were manually counted to compare the estimation with a baseline value.

harder to do as they can overlap with one another. The frame-based acquisition does not allow a single cell identification, and it is impossible to count them manually. The event-based estimation, on the other hand, manages to estimate a mean red blood cell number from the event number.

We notice that our event-based computation is slightly under estimated compared to the frame-based value. Our estimate of N_{rbc}, the mean number of event per RBC, is in real life not strictly identical over time especially in the smallest capillaries where cells are compressed and modify their shape. Fewer events are generated for one cell, and this value should decrease accordingly. In practice, the results showed a greater error when trying to adapt N_{rbc} according to the size of the capillary. Therefore, we chose to keep a fixed value despite the small under estimation.

Figure.55 shows the absolute perfusion maps for a set of vessel networks. The color corresponds again to the number of red blood cells per $100\mu m^2$. Large capillaries have, as one could expect, a higher density of red blood cells above 3 per $100\mu m^2$. Medium capillaries have a density slightly below 2rbc per $100\mu m^2$. Finally, the smallest ones have a density close to one RBC per $100\mu m^2$.

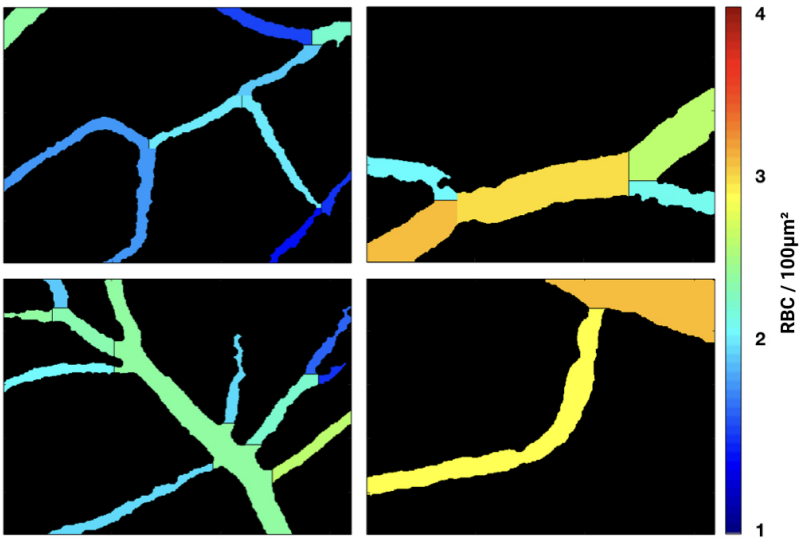

Figure 55: Screenshots of absolute perfusion maps of a mouse's cremaster in transmission microscopy using a x25 water immersion objective.

We will now focus on the relative activity map that shows the changes of activity within capillaries by comparing their current activity to a reference value (initial activity map for instance). This output provides an estimate of blood flow deregulation or degradation over time. It can serve as an indicator of hypo-perfusion or hyper-perfusion state. This type of map is particularly useful during continuous monitoring of the blood flow and to study the evolution of blood flow deregulation during a hemorrhagic shock or a vessel occlusion.

Fig.56 shows an estimation of the relative perfusion of a blood vessel with a modification of the flow. The color corresponds to a modification of the density of RBC within the vessels: if it is light green the density is constant, if it turns blue the number of RBC per $100\mu m^2$ is reduced and if it becomes red the density of erythrocytes rises. On this experiment, the right side becomes hypo-perfused while the left side is hyper-perfused locally.

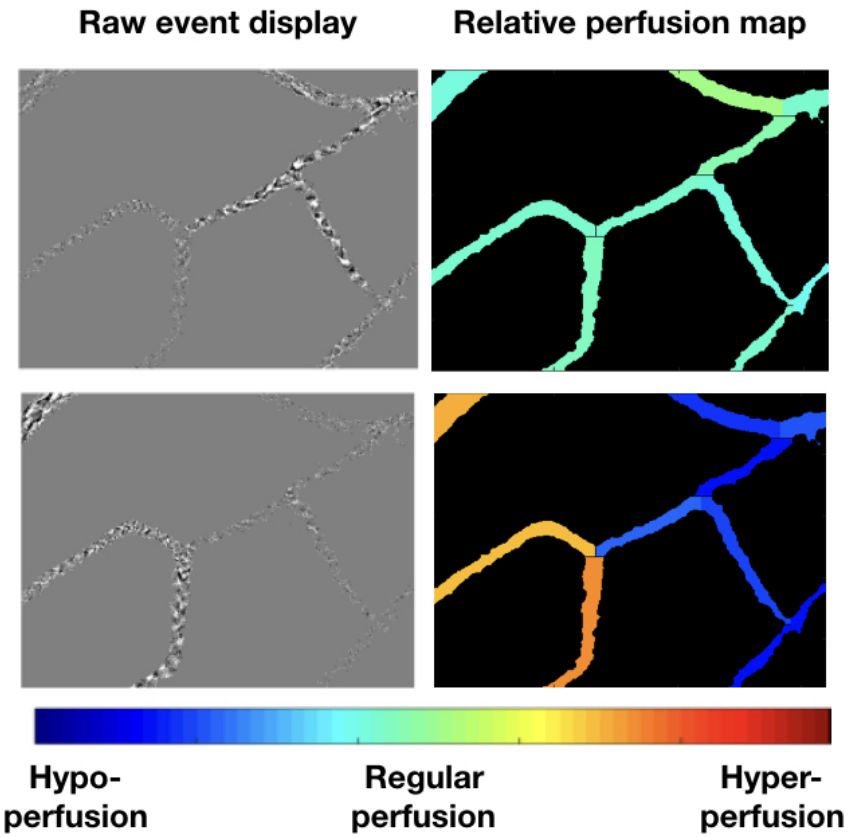

Figure 56: Relative perfusion maps of a mouse's cremaster muscle in transmission microscopy using a x25 water immersion objective. The top pictures correspond to the reference of "normal perfusion" and the bottom pictures to deregulation in blood flow.

We'll now have a look at the aftermaths following the formation of a clot. We monitor the alteration of the blood flow in a capillary network over time. Each time we display in the left column the raw event output for a time window of 100ms, in the middle the absolute density map in RBC/100μm^2 and in the right column the relative density map in RBC/100μm^2. Our reference value for the relative density map is the initial perfusion state, before the formation of the clot.

The different stages of this experiment presented on Figure.57 are the following:

- a) Initial state with normal perfusion of the whole network of capillaries. The absolute activity map shows a greater density at the base of the branch of vessels. The relative activity map is uniformly well vascular.
- b) The clot is forming outside the field of view right at the base of the main branch. The density of RBC immediately drops down to $1\text{RBC}/100\mu\text{m}^2$ (dark blue color on the absolute activity map). On the relative activity map, we observe a hypo-perfusion (light blue).
- c) The clot now completely obstructs the vessel network which is thus hypo-perfused. On the bottom right-hand corner, we see a vessel that has not been affected by the clot and remains well perfused (light green). On the left side, a small capillary is temporarily hyper-perfused (yellow color) as it tries to compensate for the lack of blood supply in the rest of the network.
- d) The clot moved upwards within the field of view and stopped at the first intersection. The circulation is back to normal on the left part of the branch.
- e) Again the clot moves upward, and a greater part of the network receives blood supply again. On the relative activity map, we clearly see that in the middle a capillary remains none vascular.
- f) The entire vessel network is normally perfused again, in a similar fashion to the initial state prior to the formation of the clot.

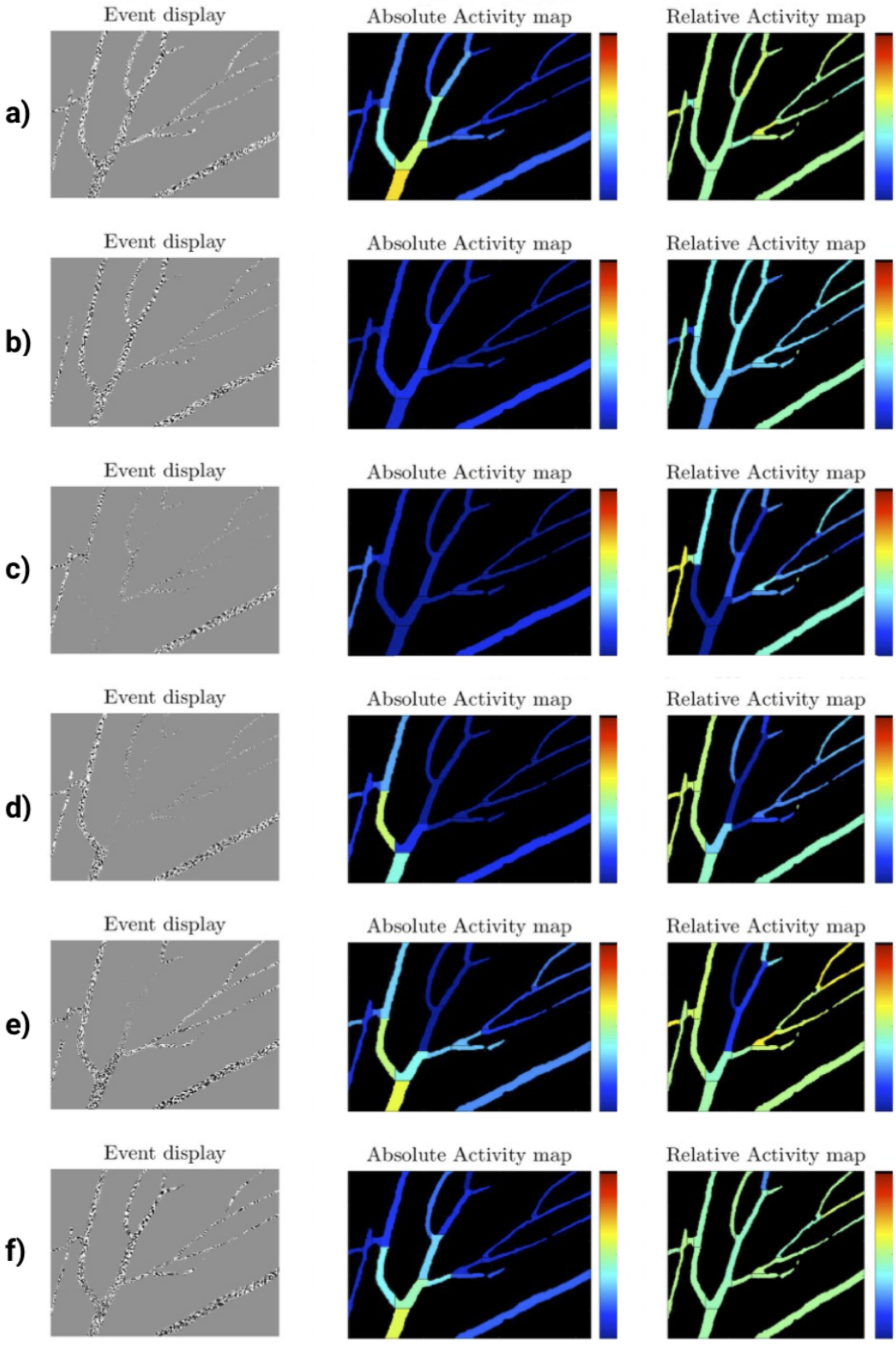

Figure 57: a) to f) Evolution of the formation and disappearance of a clot in a network of capillaries. The left column corresponds to the raw event display, the middle column displays the absolute activity map, i.e. the number of RBC/100μm^2 each second. The right column shows the evolution of the relative perfusion map with in green the initial state, in blue the hypo-perfusion and in yellow the hyper-perfusion.

5.3 RED BLOOD CELL VELOCITY

The second parameter evaluated is the velocity of red blood cells. Due to the light absorbance of erythrocytes as they cross the field of view, each cell generates a unique front of OFF events followed by a corresponding front of ON event as shown on the left on Fig.58.

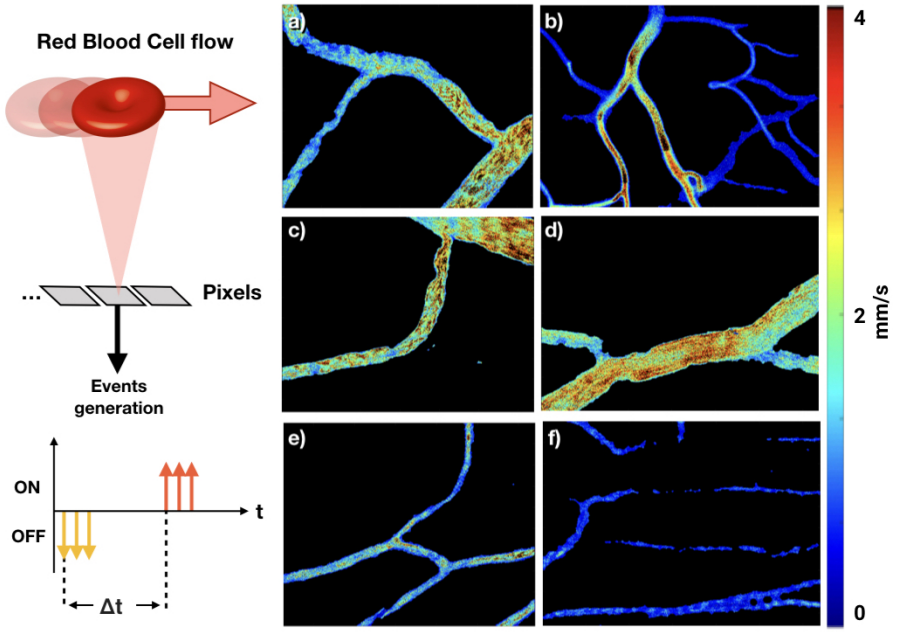

Figure 58: Left: Principle of the event-based velocity estimation for a single RBC which generates successively OFF events followed by ON events. Right: Velocity maps in capillaries arterioles and venules in mm/s.

We determine the time delay Δt between an inversion of polarity which corresponds to the time a single cell passes across a pixel. Assuming the size of a red blood cell is $s = 7\mu m$ when en-face in a capillary, we determine the velocity using:

$$v = \frac{s}{\Delta t} \tag{29}$$

We mentioned previously that over time, RBC can change shape and therefore the mean size of $7\mu m$ can change. Yet this mean value gives the best estimates (the closest to the ground truth) when computing cell velocity. Again the error in the computation may come from this estimation of the cell size, but no adaptation of the cell size has proven robust and efficient yet.

Fig.58 shows six maps of blood vessel networks with laminar flows inside small capillaries (b, e, and f) and more turbulent flows inside bigger vessels (a, c, and d).

We compared our results with a frame-based flow computed using the Lucas Kanade optical flow on 100 frames/s recording from the Hamamatsu camera. Results are shown on Fig.59.

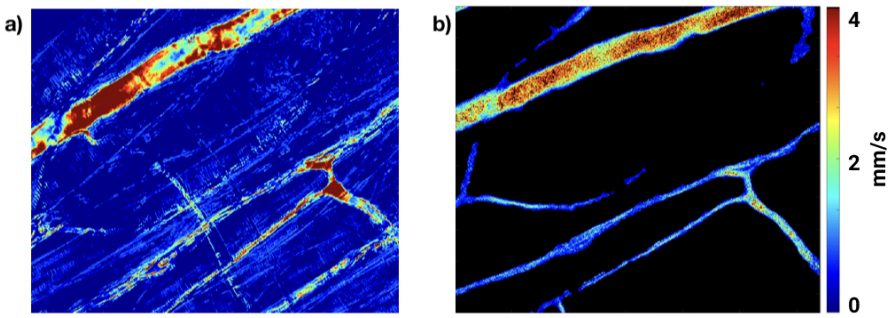

Figure 59: Velocity maps for the Hamamatsu frame-based recording (left) and our event-based algorithm (right). The absolute difference between the frame-based baseline and our estimate is below 10%.

When looking at both maps, we observe similar cell velocities in the same capillaries. Since only one camera at a time can record the blood flow, it would not be thorough to compare both maps directly. Yet we can estimate the order of magnitude for both velocities and notice an accurate correspondence between the two methods. The primary interest of these maps is to monitor the evolution of RBC speed over time to detect abnormalities if the flow increases or decreases.

We have seen how to estimate red blood cell density within capillaries by computing two types of maps: an absolute perfusion map that gives an idea of how well a network of capillaries is perfused and a relative perfusion map that highlights changes in the perfusion over time. In a second time, we have dwelt of a method to estimate red blood cell velocity within capillaries. Compared to a conventional frame based acquisition method both algorithms perform with higher accuracy as they benefit from an increased temporal resolution.

In the next section, we will focus on a practical application of microcirculation monitoring with a simulation of a hemorrhagic shock in a mouse model.

6

STUDY OF A HEMORRHAGIC SHOCK IN A MOUSE MODEL

Early this year, in January 2018, The New England Journal Of Medicine published a review article on the hemorrhagic shock which underlines that "*hemorrhage represents a substantial global problem [...] with an estimated 1.9 million deaths per year worldwide*" [8]. The hemorrhagic shock results 80% of the time from physical trauma and is, for instance, the leading cause of maternal death in the developing world[40]. Despite modern technologies, it is often lately detected and remains a substantial health issue.

A better understanding of the pathophysiology of the hemorrhagic shock has been possible thanks to animals models. There are three main categories of induced hemorrhagic shock:

- Uncontrolled shock: This model mimics a real physical trauma with spontaneous bleeding without any target volume to extract or mean arterial pressure to reach. The main drawbacks of this model are its poor replicability as well as the difficulty to resuscitate the animal afterwards.
- Volume controlled shock: This time, a fixed volume of blood is extracted depending on the animal weigh. The main drawback of this model is its inter-subject variability.
- Pressure-controlled shock: A fixed mean arterial pressure value is reached via the extraction of a volume of blood. Once this value is attained, animals are maintained at this level before being resuscitated.

In this chapter, we induce a pressure controlled hemorrhagic shock in a mouse with initial exsanguination and continuous monitoring of the Mean Arterial Pressure (MAP). This model of a controlled hemorrhagic shock has initially been developed by Wiggers on dogs [71, 72]. Once the desired MAP is reached, the animals are maintained in this state for a fixed duration before being transfused back with the blood volume that was removed. The aim is to observe the degradation of the micro-circulation and estimate the correlation between the state of the animal and the hemodynamics of the micro-circulation. In order to do so, we measure the activity of blood vessels and the RBC velocity over time.

6.1 SURGICAL PROCEDURE

We induce a hemorrhagic shock in a mouse by reducing its global blood volume thanks to a syringe filled with saline and connected to an artery. Throughout the experiment, we measure the systemic arterial blood pressure (MAP) of the animal. Initially, its value is 52mmHg, and the blood flow is homogeneous. Our field of view is locked on a network of capillaries, and we will monitor both the evolution of the density and speed of RBC during the shock and after resuscitation. At $t = 0mn$, we lower the MAP progressively to 32 by removing blood with the syringe. Every 5mn we measure the density and speed of the erythrocytes. After 30mn, we re-inject fluids into the mouse through the catheter until the MAP stabilizes around its original value. A schematic of the setup is shown on Figure.60

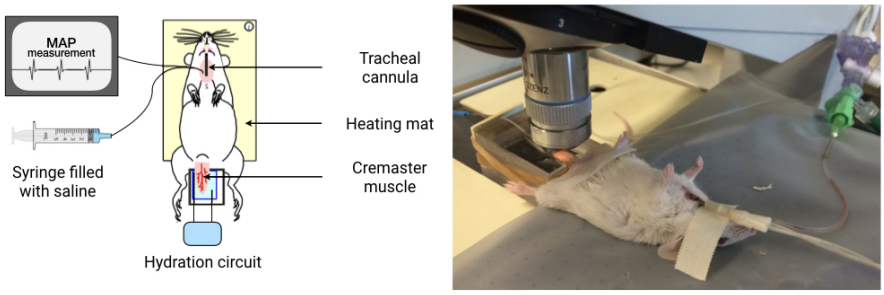

Figure 60: Schematics of the setup used to observe capillaries on the external layer of the cremaster muscle. The mouse is in supine position.

6.2 RESULTS

On Table.4 is shown the evolution of the MAP during the experiment.

TIME (MN)	0	5	10	15	20	25	30	35	40
MAP	52	42	32	32	33	33	34	41	51

Table 4: Evolution of the systemic arterial blood pressure through a hemorrhagic shock. At $t = 0mn$, the mouse's blood volume is reduced and its MAP drops. At $t = 30mn$, the mouse is re-injected with fluids.

We follow the same methodology as previously described in section 5.2. Every five minute, we compute the mean number of RBC per $100\mu m^2$ per ms during a one-minute recording. The result are displayed on Figure.61. The red bars at the bottom correspond to the mean number of RBC per $100\mu m^2$ each ms and the black line on top

to the evolution of the MAP over time. When the MAP drops after 0mn, the density of RBC decreases from 2.5 to 1.5 after 5mn and stabilizes around 0.5 after 10mn. Between $20-25$mn we see that the MAP starts to increase while the density of erythrocytes briefly rises to 1 before plummeting again. We believe that the MAP increase is due to a compensation phenomenon from the mouse. This will be further detailed in the discussion. After 30mn, we initiate the resuscitation of the mouse. We observe that the MAP increases back to its original value and the density of RBC rises again slightly above 2RBC per $100\mu m^2$ each ms.

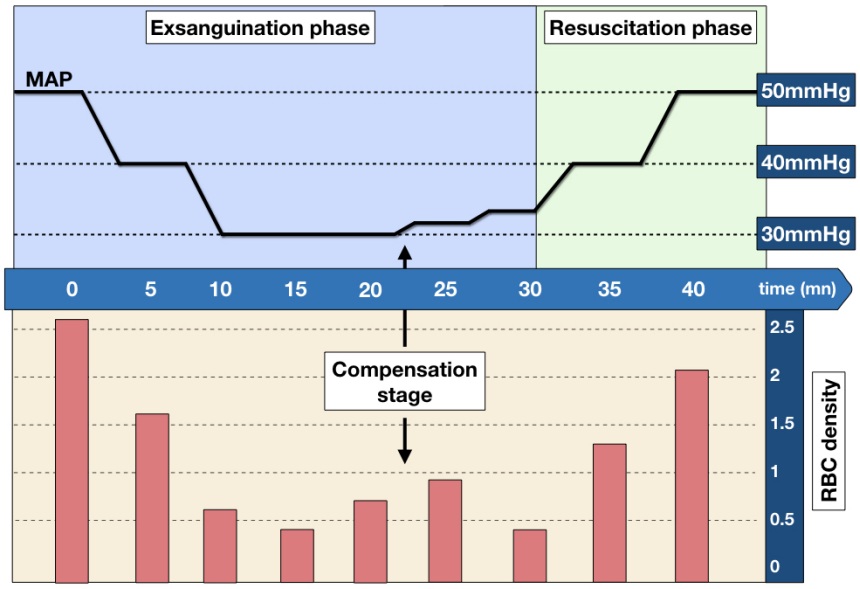

Figure 61: Evolution of the density of RBC per $100\mu m^2$ per ms within capillaries during a hemorrhagic shock. At $t = 0$mn the internal blood volume is reduced and the density drops. At $t = 30$mn the mouse is resuscitated.

On Figure.62 are shown the variations of the RBC density during a one-minute recording at 0mn, 10mn, 20mn, 30mn and 40mn. We see that when the MAP is at a normal value, the fluctuations are regular with a small disparity (initially $\sigma_{0mn} = 0.048$ and after the resuscitation $\sigma_{40mn} = 0.057$). This characterizes a homogeneous blood flow. When the micro-circulation degrades, the density of RBC drops and the variations come close to zero (no blood flow) with random heterogeneous fluctuations (circled in yellow) with greater disparities ($\sigma_{10mn} = 0.074$ at the start of the hemorrhage, $\sigma_{20mn} = 0.061$ during the compensation stage and $\sigma_{30mn} = 0.099$ when the density of erythrocytes is the lowest).

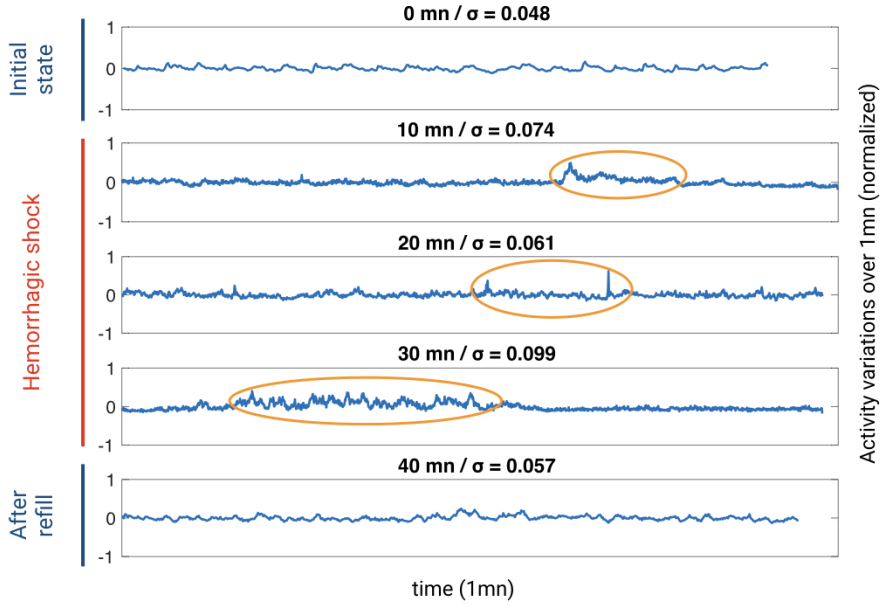

Figure 62: Normalized variations of the density of RBC per$100\mu m^2$ during a one minute recording. The σ values represent the heterogeneity of the fluctuations. The smaller σ is, the more homogeneous are the variations. The yellow circles highlight the heterogeneous fluctuations during the hemorrhage.

Let us now have a look at the speed of RBC within capillaries during the hemorrhagic shock. We expect the variations of the speed to change according to the density of RBC.

On Figure.63 are shown five snapshots of the speed map in our region of interest. The colormap corresponds to the speed of red blood cells in mm/s. At $0mn$ the network is well perfused and the flow is homogeneous within capillaries. $15mn$ after the beginning of the hemorrhage, the MAP is $30mmHg$ and we see that small vessels turn blue which means that the RBC's velocity decreases. We notice however that large vessels remain well perfused. After $30mn$, most RBC are at a standstill (dark blue capillaries): the blood flow has stopped in most regions. We resuscitate the mouse after $30mn$ of hemorrhage and $15mn$ later the RBC have similar speed to the original state.

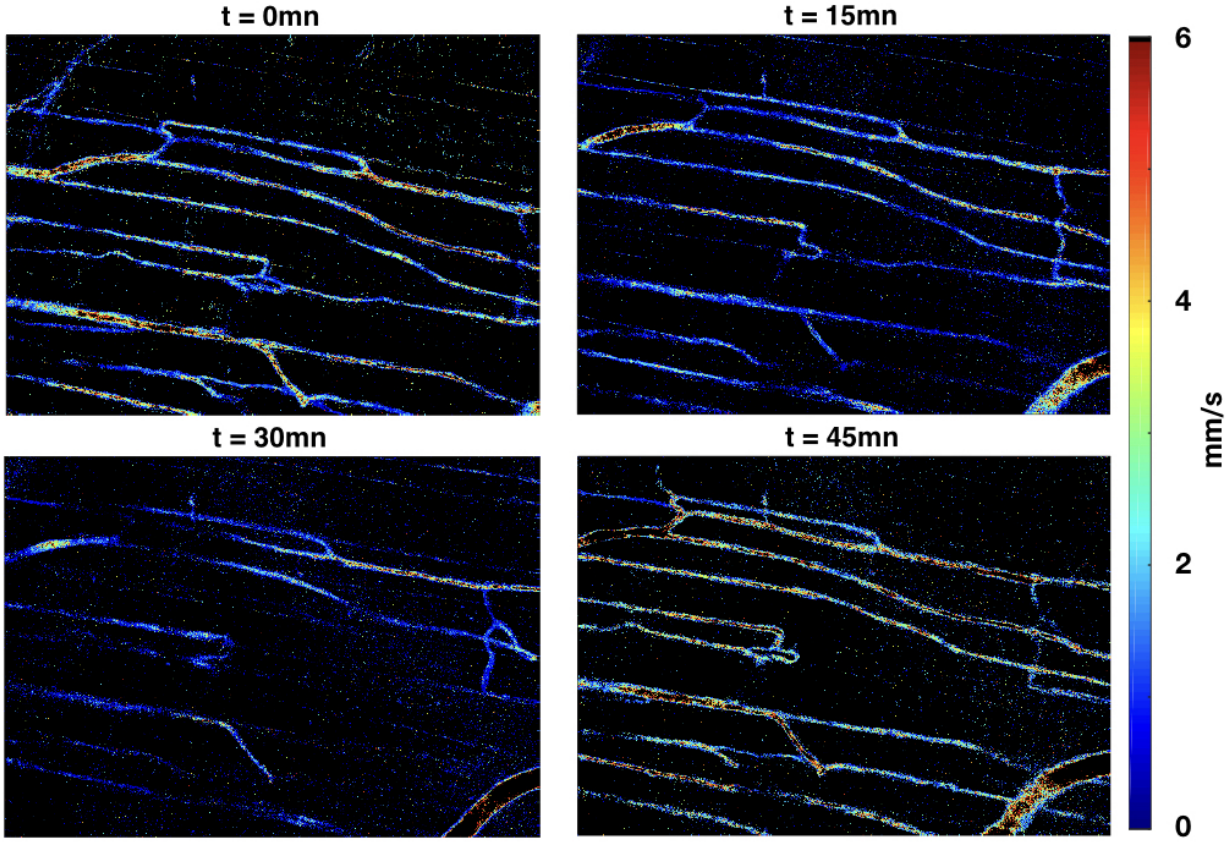

Figure 63: Evolution of the RBC's speed over time during a hemorrhagic shock. At omn the network is well perfused. 15mn after the beginning of the hemorrhage, the RBC's velocity decreases in all the capillaries. After 30mn, most RBC are at a standstill (dark blue capillaries). 15mn after the reperfusion of the mouse, the RBC have similar speed to their original state. The color bar corresponds to the speed of RBC in mm/s.

6.3 DISCUSSION

Regarding the activity of capillaries, we clearly see with this experiment that the micro-circulation degrades rapidly during a hemorrhagic shock. The density of RBC inside capillaries drops within minutes and presents heterogeneous variations as opposed to the small disparities when the blood flow is homogeneous. We notice a correlation between the MAP and the activity of capillaries within the first 20mn, after which the MAP rises despite the fact that the micro-circulation remains altered. This phenomenon known as compensation was described by *Wiggers et al.* who identified three outcomes after a quick hemorrhage:

- First outcome: after a loss of $30-40\%$ of their blood volume, the animals were able to spontaneously recover thanks to compensation mechanisms (without any transfusion or resuscitation).
- Second outcome: after a loss of more than 40% of their blood volume and if no cardiac arrest has occurred, anoxia with irreversible cellular damages develops. Survival is possible with a suited resuscitation. This state is called "imminent shock".
- Third outcome: the MAP keeps dropping, and the only solution is a re-transfusion of the animals which is often very effective on the short term. Indeed, the health improvement is only temporary, and the state of the animals deteriorate in a second time. This state is the "irreversible shock".

When there is a correlation between the micro-circulation and the MAP we can still expect the first outcome. If the macro-circulation improves (i.e. the MAP rises), whether the animal is compensating or it is transitioning to the state of imminent shock. The study of the micro-circulation is here of the utmost importance as it may enable the distinction between these two outcomes [33]. Here we see the MAP rising while the activity of capillaries remains below normal. The correlation is lost, and the animal is in a state of imminent shock and must be immediately resuscitated to avoid irreversible damages.

The velocity information is in line with the density of RBC and can serve as a second clue to determine a state of imminent shock. Additionally, we notice that some capillaries initially well perfused are no longer supplied with blood after resuscitation. On the opposite, a few small vessels that were not perfused are now vascular after resuscitation. A possible explanation is that during the hemorrhage, the organism of the mouse has re-organized its blood supply with the regions that remained the most vascular and kept this re-rooting after resuscitation. This is however a hypothesis, and an extensive work studying this particular phenomenon should be carried out.

CONCLUSION

AN OUNCE OF PREVENTION IS WORTH A POUND OF CURE

We have demonstrated how neuromorphic sensors can give new insights into medical imaging in particular in the study of hemodynamics. The FFOCT technique is the best candidate to study in depth, in a non-invasive way, the dynamics of RBC. The coupling of an event-based sensor with a FFOCT microscope has allowed the estimation of optical flows for single particles up to $6ml/h$ at the cellular level. We have also demonstrated the capabilities of our setup to determine concentrations up to 30 000 $particles/ml$, going beyond the current limitations of frame-based acquisition systems in real time. However, cameras still need improvement in order to take the full advantage of the technique: smaller pixels in order to observe biological structures at the cellular scale with a larger field of view and a cooling system to reduce thermal noise to its minimum.

The cooled biomimetic sensor presented in the second chapter of this thesis showed improvements compared to the Atis camera when dealing with low contrast variations and low levels of light. The increase in SNR enabled a finer tuning of the event-based algorithms. In turn, we were able to push further the limitations previously encountered when estimating velocities and densities. The micro-circulation device presented in chapter 5 is a promising tool to have a rapid glimpse of the dynamic morphological parameters of erythrocytes. This prototype however still requires a few improvements regarding its bulky size. Indeed, the light sources, as well as electronics, used take too much space today for a portable device.

Finally, we have shown how both the activity map and the velocity map of capillaries provide, during a hemorrhagic shock, relevant information and can serve as early clues to detect a deterioration of the micro-circulation. Within minutes, a degradation is noticeable, and we observe both a reduction of the density of RBC inside capillaries as well as a decrease of the flow. There is, at this point, a direct correlation between the micro-circulation hemodynamics and the mean arterial pressure (MAP) of the animal. Later on, the MAP rises while we notice no improvement of the micro-circulation. This decorrelation may indicate a change of state, and more precisely, we hypothesize that the information from the micro-circulation coupled with macro-data can determine the moment of an imminent shock.

The potential of this technique is not limited to hemorrhage detection only. Indeed the "state of shock" in general, defined as an insufficient blood circulation leading to tissues hypoxia, alters the microcirculation in many ways. From a physio-pathological point of view, this defect in tissue perfusion can have the following causes:

- An absolute hypovolemia due to a hemorrhagic shock as we have studied in this work.
- A relative hypovolemia characterized by a vasoplegia as in an anaphylactic shock.
- A failure of the cardiac pump which leads to a reduction of the cardiac output as in a cardiogenic shock.
- Cardiac irregularities which lead to heterogeneous blood flow as in a septic shock.

No matter the origin, the state of shock represents a life-threatening emergency which requires a fast diagnosis to provide immediate care. The use of neuromorphic cameras coupled with the proper imaging device offers the possibility to process the information from hemodynamics instantly. Extensive work on the different types of shock is an appealing idea in order to determine if, similarly to the hemorrhagic shock, they can be predicted.

The primary perspective for the future is to further develop the micro-circulation device and make it commercially available. Many steps will be required as this is still an experimental prototype. First, we need to focus our attention on fully calibrating and validating the results provided by the device. Part of this work needs to include a complete study of the different types of shock and their consequences on the micro-circulation. A user-friendly software needs to be created as well in order to have easy access to the data. Then clinical trials will be necessary before thinking about a commercial version of the device. Finally, a miniaturization step may be required in order to make a pocket-size setup that is easy to handle.

In this thesis, we have focused on micro-circulation monitoring related to the state of shock. There are numerous other applications which could benefit from accurate monitoring of the micro-circulation. For instance, right after a transplant, there are currently no technique to estimate how well the new organ is perfused. Clinicians wait for the kidney to turn pink which indicates that the blood flow is established before closing the patient. After that a careful monitoring of the patient's vitals over an extended period of time is necessary in order to determine if the transplant was successful. If not, the patient needs to be re-opened and the organ replaced. Our device could provide information more explicitly with real live feedback on the micro

hemodynamics right after the transplant. We believe this could reduce the number of failed transplant if clinicians could directly see, before closing the patient, that the micro-circulation is not established. Another example is with diabetic patients: with a dual wavelength illumination on the capillaries, it would be possible to estimate the level of oxygen and sugar contained in their blood, and easily adapt treatments accordingly.

More generally speaking, I believe that asynchronous sensors and event-based computation have a key role to play in medical imaging. Frame-based devices are improving daily, with an increased temporal resolution which means more frames and an increased spatial resolution with smaller pixels. As a result, the amount of data recorded, stored and processed is getting more and more substantial. This has a cost. It is both more energy intensive and expensive to deal with this information. Now more than ever we need to think about reducing expenses as well as our carbon emissions. Neuromorphic vision sensors are low power, and as they record the information asynchronously based on the light changes in the scene, the amount of information stored is reduced without losing signal. They are today the most energy efficient device to record information with a high temporal precision. It is essential that they take a more significant part in medical imaging in order to become widely used and be part of tomorrow's new generation of scanners.

BIBLIOGRAPHY

[1] In: (). URL: https://www.nlm.nih.gov/exhibition/historicalanatomies/bougle_home.html.

[2] C. Apelian, F. Harms, O. Thouvenin, and C. Boccara. "Dynamic full field optical coherence tomography: subcellular metabolic contrast revealed in tissues by interferometric signals temporal analysis." In: *Biomedical Optics Express* 7 (2016), pp. 1511–1524.

[3] N. Baudry, E. Laemmel, and E. Vicaut. "In Vivo Reactive Oxygen Species Production Induced By Ischemia In Muscle Arterioles Of Mice: Involvement Of Xanthine Oxidase And Mitochondria." In: *American Journal of Physiology, Heart and Circulatory Physiology* 294 (2008), pp. 821–828.

[4] N. Baudry, G. Danialou, J. Boczkowski, and E. Vicaut. "In Vivo Study Of The Effect Of Systemic Hypoxia On Leukocyte-Endothelium Interactions." In: *American Journal of Respiratory and critical care Medicine* 158 (1998), pp. 477–483.

[5] R. Benosman, S.-H. Ieng, C. Clercq, C. Bartolozzi, and M. Srinivasan. "Asynchronous Frameless Event-Based Optical Flow." In: *Neural Networks* 27 (2012), pp. 32–37.

[6] R. Benosman, C. Clercq, X. Lagorce, S. H. Ieng, and C. Bartolozzi. "Event-Based Visual Flow." In: *IEEE Transactions on Neural Networks* 25 (2014), pp. 407–417.

[7] X. Berthelon, G. Chenegros, N. Libert, J.A. Sahel, Grieve K., and R. Benosman. "Full-field OCT Technique For High Speed Event-based Optical Flow And Particle Tracking." In: *Optics Express* 25 (2017), pp. 12611–12621.

[8] J.W. Cannon. "Hemorrhagic Shock." In: *The New England Journal of Medicine* 378 (2018), pp. 370–379.

[9] E. Chaigneau, M. Oheim, E. Audinat, and S. Charpak. "TwoPphoton Imaging Of Capillary Blood Flow In OlfactoryProceedings of the National Academy of Sciences." In: 100 (2003), pp. 13081–13086.

[10] S.-L. Chen, Z. Xie, P. L. Carson, X. Wang, and L. J. Guo. "In Vivo Flow Speed Measurement Of Capillaries By Photoacoustic Correlation Spectroscopy." In: *Optics Letter* 36 (2011), pp. 4017–4019.

[11] "Clinical Review: Clinical Imaging Of The Sublingual Microcirculation In The Critically Ill - WhereDo We Stand?" In: *Critical Care* 16 (2012), pp. 224–233.

[12] E. Culurciello, R. Etienne-Cummings, and K.A. Boahen. "A biomorphic digital image sensor." In: *IEEE Journal of Solide-State Circuits* 38 (2003), pp. 281–294.

[13] D. De Backer, J. Creteur, J.C. Preiser, M.J. Dubois, and J.L. Vincent. "Microvascular Blood Flow Is Altered In Patients With Sepsis." In: *American Journal of Respiratory and Critical Care Medecine* 166 (2002), pp. 100–104.

[14] A. Dubois, L. Vabre, C. Boccara, and E. Beaurepaire. "High-Resolution Full-Field Optical Coherence Tomography With A Linnik Microscope." In: *Applied Optics* 41 (2002), pp. 805–812.

[15] A. Dubois, K. Grieve, G. Moneron, R. Lecaque, L. Vabre, and C. Boccara. "Ultrahigh-Resolution Full-Field Optical Coherence Tomography." In: *Applied Optics* 43 (2004), pp. 2874–2883.

[16] T. Durduran, G. Yu, M.G. Burnett, J.A. Detre, J.H. Greenberg, J. Wang, C. Zhou, and A.G. Yodh. "Diffuse Optical Measurement Of Blood Flow, Blood Oxygenation, And Metabolism In A Human Brain During Sensori Motor Cortex Activation." In: *Optics Letter* 29 (2004), pp. 1766–1768.

[17] S. Eriksson, J. Nilsson, and C. Stureson. "Non-Invasive Imaging Of Microcirculation: A Technology Review." In: *Medical Devices: Evidence and Research* 7 (2014), pp. 445–452.

[18] P. T. Goedhart, M. Khalilzada, R. Bezemer, J. Merza, and C. Ince. "Sidestream Dark Field (SDF) Imaging: A Novel Stroboscopic LED Ring-based Imaging Modality For Clinical Assessment Of The Microcirculation." In: *Optics Express* 15 (2007), pp. 101–114.

[19] W. Groner, J.W. Winkelman, A.G. Harris, C. Ince, G.J. Bouma, K. Messmer, and R.G. Nadeau. "Orthogonal Polarization Spectral Imaging: A New Method For Study Of The Microcirculation." In: *Nature Medicine* 5 (1999), pp. 1209–1212.

[20] G. Gutierrez, H.D. Reines, and M.E. Wulf-Gutierrez. "Clinical Review: Hemorrhagic Shock." In: *Critical Care* 8 (2004), pp. 373–381.

[21] R. Haindl, A. Wartak, W. Trasischker, S. Holzer, B. Baumann, M. Pircher, C. Vass, and C. K. Hitzenberger. "Total Retinal Blood Flow In Healthy And Glaucomatous Human Eyes Measured With Three Beam Doppler Optical Coherence Tomography." In: *Biomedical Optics Express* TTh1B.2 (2016).

[22] R. He-Sheng. "Construction of a Generalized Psychrometric Chart for Different Pressures." In: *International Journal of Mechanical Engineering Education* 32 (2004), pp. 212–222.

[23] D. Huang et al. "Optical Coherence Tomography." In: *Science* 22 (1991), pp. 1178–1181.

[24] C. Ince. "The Microcirculation Is The Motor Of Sepsis." In: *Critical Care* 9 (2005), pp. 13–19.

[25] J.A. Izatt, S. Boppart, B. Bouma, J. de Boer, W. Drexler, X. LI, and Y. Yasuno. "Introduction To The Feature Issue On The 25 Year Anniversary Of Optical Coherence Tomography." In: *Biomedical Optics Express* 8 (2017), p. 3289.

[26] Y. Jia, J. C. Morrison, J. Tokayer, O. Tan, L. Lombardi, B. Baumann, C. D. Lu, W. Choi, J. G. Fujimoto, and D. Huang. "Quantitative Oct Angiography Of Optic Nerve Head BloodFflow." In: *Biomedical Optics Express* 3 (2012), pp. 3127–3137.

[27] X. Lagorce, C. Meyer, S. H. Ieng, D. Filliat, and R. Benosman. "Asynchronous Event-Based Multikernel Algorithm For High-Speed Visual Features Tracking." In: *IEEE Transactions on Neural Networks* 26 (2015), pp. 1710–1720.

[28] J. Lee, W. Wu, J. Y. Jiang, B. Zhu, and D. A. Boas. "Dynamic Light Scattering Optical Coherence Tomography." In: *Optics Express* 20 (2012), pp. 22262–22277.

[29] J. Lee, W. Wu, F. Lesage, and D. A. Boas. "Multiple Capillary Measurement Of Rbc Speed, Flux, And Density With Optical Coherence Tomography." In: *Journal of Cerebral Blood Flow Matebolism* 33 (2013), pp. 1707–1710.

[30] R.A. Leitgeb, L. Schmetterer, W. Drexler, A.F. Fercher, R.J. Zawadzki, and T. Bajraszewski. "Real-Time Assessment Of Retinal Blood Flow With Ultrafast Acquisition By Color Doppler Fourier Domain Optical Coherence Tomography." In: *Optics Express* 11 (2003), pp. 3116–3121.

[31] C.E. Leroux, F. Bertillot, O. Thouvenin, and C. Boccara. "Intracellular dynamics measurements with full field optical coherence tomography suggest hindering effect of actomyosin contractility on organelle transport." In: *Biomedical Optics Express* 7 (2016), pp. 4501–4513.

[32] P. Li, S. Ni, L. Zhang, S. Zeng, and Q. Luo. "Imaging Cerebral Blood Flow Through The Intact Rat Skull With Temporal Laser Speckle Imaging." In: *Optics Letter* 31 (2006), pp. 1824–1826.

[33] N. Libert, A. Harrois, and J. Duranteau. "Haemodynamic coherence in haemorrhagic shock." In: *Best Practice and Research Clinical Anaesthesiology* 30 (2016), pp. 429–435.

[34] N. Libert, A. Harrois, N. Baudry, E. Vicaut, and J. Duranteau. "Intestinal Microcirculation And Mucosal Oxygenation During Hemorrhagic Shock And Ressucitation At Different Inspired Oxygen Concentration." In: *Journal of Trauma and Acute Care Surgery* 83 (2017), pp. 476–484.

[35] P. Lichtsteiner and T. Delbruck. "A 64X64 AER Logarithmic Temporal Derivative Silicon Retina." In: *Research in Microelectronics and Electronics* 2 (2005), pp. 202–205.

[36] P. Lichtsteiner, C. Posch, and T. Delbruck. "A 128X128 dB 15Microsecond Latency Asynchronous Temporal Contrast Vision Sensor." In: *IEEE journal of Solid-State Circuits* 43 (2008), pp. 566–576.

[37] Huei-Yung Lin and Chia-Hong Chang. "Depth recovery from motion and defocus blur." In: *Image Analysis and Recognition* (2006), pp. 122–133.

[38] M. Mahowald. "VLSI analogs of neuronal visual processing: a synthesis of form and function." In: *PhD Thesis, California Institute of Technology* (1991).

[39] M. Mahowald and R. Douglas. "A Silicon Neuron." In: *Nature* 354 (1991), p. 515.

[40] Marie-Jocelyne Martel, Katherine Jane MacKinnon, Marc-Yvon Arsenault, Elias Bartellas, Michael C Klein, Carolyn A Lane, Ann E Sprague, and Ann Kathleen Wilson. "Hemorrhagic Shock." In: *Journal of obstetrics and gynaecology Canada* 24 (2002), pp. 504–521.

[41] V. Mazlin, P. Xiao, J. Scholler, K. Grieve, K. Irsch, J.A. Sahel, M. Fink, and C. Boccara. "Ultra-high Resolution Full-field OCT (FFOCT) For Cornea And Retina." In: *Imaging and Applied optics* (2018).

[42] D. E. McMillan. "Deterioration Of The Microcirculation In Diabetes." In: *Diabetes* 24.10 (1975), pp. 944–957.

[43] E. Meijering, O. Dzyubachyk, and I. Smal. "Methods For Cell And Particle Tracking." In: *Methods in Enzymology* 504 (2012), pp. 183–200.

[44] Z. NI, C. Pacoret, R. Benosman, S. Ieng, and S. Regnier. "Asynchronous Event-Based High Speed Vision For Microparticle Tracking." In: *Journal of Microscopy* 245 (2012), pp. 236–244.

[45] Y. Nakajima, N. Baudry, J. Duranteau, and E. Vicaut. "Microcirculation In Intestinal Villi." In: *American Journal of Respiratory and Critical care Medicine* 164 (2001), pp. 1526–1530.

[46] A. Nakano, Y. Sugii, M. Minamiyama, and H. Niimi. "Measurement Of Red Cell Velocity In Microvessels Using Particle Image Velocimerty (PIV)." In: *Clinical hemorheology and microcirculation* 29 (2003), pp. 445–455.

[47] Z. Ni, S.H. Ieng, C. Posch, S. Regnier, and R. Benosman. "Visual tracking using neuromorphic asynchronous event-based cameras." In: *Neural Computation* 27 (2015), pp. 925–953.

[48] A.P. Pentland, S. Scherock, T. Darrel, and B. Girod. "Simple Range Cameras Based On Focal Error." In: *Optical Society of America* 11 (1994), pp. 2925–2934.

[49] C. Posch and D. Matolin. "Sensitivity And Uniformty Of A 0.18Micrometer CMOS Temporal Contrast Pixel Array." In: *Circuits and Systems (ISCAS), 2011 IEEE International Symposium on* (2011), pp. 1572–1575.

[50] C. Posch, D. Matolin, and R. Wohlgenannt. "High-dr Frame-Free Pwm Imaging With Asynchronous Aer Intensity Encoding And Focal Plane Temporal Redundancy Suppression." In: *Proceedings of 2010 IEEE International Symposium on Circuits and Systems* (2010), pp. 2430–2433.

[51] C. Posch, D. Matolin, and R. Wohlgenannt. "A QVGA 143 dB Dynamic Range Frame-Free PWM Image Sensor With Lossless Pixel-Level Video Compression And Time-Domain CDS." In: *IEEE Journal of solid-state circuits* 46 (2011), pp. 259–275.

[52] C. Posch, D. Matolin, R. Wohlgenannt, M. Hofstatter, P. Schon, M. Litzenberger, D. Bauer, and H. Garn. "Biomimetic Frame-free HDR Camera With Event-driven PWM Image Video Sensor And Full-custom Address-event Processor." In: *2010 IEEE Biomedical Circuits and Systems Conference* (2010), pp. 254–257.

[53] C. Posch, T. Serrano-Gotarredona, B. Linares-Barranco, and T. Delbruck. "Retinomorphic event-based vision sensors: bioinspired cameras with spiking output." In: *Proceedings of the IEEE* 102 (2014), pp. 1470–1484.

[54] D. Reverter Valeiras, X. Lagorce, X. Clady, C. Bartolozzi, S.H. Ieng, and R. Benosman. "An asynchronous neuromorphic event-driven visual part-based shape trakcing." In: *IEEE transaction on neural netwroks and learning systems* 26 (2015), pp. 3045–3059.

[55] Y. Sakr, M.J. Dubois, D.l De Backer, J. Creteur, and J.L. Vincent. "Persistent Microcirculatory Alterations Are Associated With Organ Failure And Death In Patients With Septic Shock." In: *Critical Care Medicine* 32 (2004), pp. 1825–1831.

[56] J.S. Schuman, C.A. Puliafito, J.G. Fujimoto, and J.S. Duker. "Optical Coherence Tomography Of Ocular Dsiaeases 3rd Edition." In: *Optical coherence of Ocular diseases* (2004).

[57] N. Segal et al. "Improving Microcirculation With Therapeutic Intrathoracic Pressure Regulation In A Porcine Model Of Hemorrhage." In: *Resuscitation* 82 (2011), pp. 16–22.

[58] V.J. Srinivasan, H. Radhakrishnan, E.H. Lo, E.T. Mandeville, J.Y. Jiang, S. Barry, and A. E. Cable. "OCT Methods For Capillary Velocimetry." In: *Biomedical Optics Express* 3 (2012), pp. 612–629.

[59] W. D. Strain and P. M. Paldanius. "Diabetes, Cardiovascular Disease And The Microcirculation." In: *Cardiovascular Diabetology* 17 (2018), p. 57.

[60] P. Swain and D. Cheskis. "Back-Illuminated Image Sensors Come To The Forefront-Novel Materials And Fabrication Methods Increase Quality And Lower Cost Of Sensors For Machine Vision And Industrial Imaging." In: *Photonics Spectra* 42 (2008), p. 46.

[61] J. Szopinski, K. Kusza, and M. Semionow. "Microcirculatory Responses To Hypovolemic Shock." In: *Journal of Trauma and Acute Care Surgery* 71 (2011), pp. 1779–1788.

[62] G. Tachon, A. Harrois, S. Tanaka, H. Kato, O. Huet, J. Pottecher, E. Vicaut, and J. Duranteau. "Microcirculatory Alterations in Traumatic Hemorrhagic Shock." In: *Critical Care Medicine* 42 (2014), pp. 1433–1441.

[63] S. Tanaka, A. Harrois, C. Nicolai, M. Flores, S. Hamada, E. Vicaut, and J. Duranteau. "Qualitative real-time analysis by nurses of sublingual microcirculation in intensive care unit: the MICRONURSE study." In: *Critical care* 19 (2015).

[64] O. Thouvenin, M. Fink, and C. Boccara. "Dynamic multimodal full-field optical coherence tomography and fluorescence structured illumination microscopy." In: *Journal of Biomdeical Optics* 22 (2017).

[65] S. Trzeciak, R.P. Dellinger, J.E. Parrillo, M. Guglielmi, J. Bajaj, N.L. Abate, R.C. Arnold, S. Colilla, S. Zanotti, and S.M. Hollenberg. "Early Microcirculatory Perfusion Derangements In Patients With Severe Sepsis And Septic Shock: Relationship To Hemodynamics, Oxygen Transport, And Survival." In: *Annals of Emergency Medicine* 49 (2007), pp. 88–98.

[66] L.G. Ungerleider and J.V. Haxby. "What And Where In The Human Brain." In: *Current Opinion in Neurobiology* 4 (1994), pp. 157–165.

[67] Z. Uz, C. Ince, P. Guerci, Y. Ince, R.P. Araujo, B. Ergin, M.P. Hilty, T.M. van Gulik, and B.A. de Mol. "Recruitment Of Sublingual Microcirculation Using Handheld Incident Dark Field Imaging As A Routine Measurement Tool During The Postoperative De-escalation Phase - A Pilot Study In Post ICU Cardiac Surgery Patients." In: *Perioperative Medicine* 7 (2018).

[68] L. Vabre, A. Dubois, and C. Boccara. "Thermal-light Full-Field Optical Coherence Tomography." In: *Optics Letters* 27 (2002), pp. 530–532.

[69] Z. Wan, S. Sun, G. Ristagno, M.H. Weil, and W. Tang. "The Cerbral Microcirculation Is Protected During Experimental Hemorrhagic Shock." In: *Critical care Medecine* 38 (2010), pp. 928–932.

[70] M. Watanabe and S.K. Nayar. "Rational Filters For Passive Depth From Defocus." In: *Int J Comput Vis.* 27 (1997), pp. 203–225.

[71] C.J. Wiggers. "The Present Status Of The Shock Problem." In: *Physiological Reviews* 22 (1942), pp. 74–123.

[72] H.C. Wiggers and R.C. Ingraham. "Hemorrhagic Shock: Definition And Criteria For Its Diagnosis." In: *The journal of clinical investigation* 25 (1946), pp. 30–36.

[73] P. Xiao, M. Fink, and C. Boccara. "Combining FF-OCT With SD-OCT For Retinal Imaging." In: *Proceedings of SPIE-OSA* 10416 (2017).

[74] C. Zhou, S. Lin, and S. Nayar. "Coded Aperture Pairs For Depth From Defocus And Defocus Blurring." In: *Int J Comput Vis.* 93 (2011), pp. 53–69.